Nonlinear responses and three-particle correlators in correlated electron systems exemplified by the Anderson impurity model

Patrick Kappl ⬤, Friedrich Krien ⬤, Clemens Watzenböck ⬤, and Karsten Held ⬤

Institute of Solid State Physics, TU Wien, 1040 Vienna, Austria

Three-particle correlators are relevant for, among others, Raman, Hall, and nonlinear responses. They are also required for the next order of approximations extending dynamical mean-field theory diagrammatically. We present a general formalism on how to treat these three-particle correlators and susceptibilities, and we calculate the local three-particle response of the Anderson impurity model numerically. We find that genuine three-particle vertex corrections are sizable. In particular, it is not sufficient to just take the bare bubble terms or corrections based on the two-particle vertex. The full three-particle vertex must be considered.

I. INTRODUCTION

Our physical understanding is very much based on one-particle and two-particle Green's functions, upon which books on quantum field theory generally focus [1]. On the one-particle level, we understand quasiparticle renormalizations and lifetimes, metal-insulator transitions, as well as magnetic ordering in the symmetry-broken phase. The one-particle Green's function and self-energy are also at the heart of dynamical mean field theory (DMFT) [2–5], which calculates the self-energy by (self-consistently) summing up the local contribution of all Feynman diagrams [2]. Hence, it is maybe not surprising that the success of DMFT had a focus on describing the aforementioned one-particle properties such as quasiparticle renormalizations and the Mott-Hubbard metal-insulator transition.

On the two-particle level, we have the two-particle Green's function from which we can calculate physical responses such as the magnetic or charge susceptibility. Here, the two-particle vertex plays the role of the self-energy. It describes all physics beyond a rather trivial bare bubble susceptibility that is akin to the noninteracting case, only now with renormalized one-particle Green's function lines. On this two-particle level there has been some recent progress to describe electronic correlations—brought about through diagrammatic extensions of DMFT [6–12]; for a review, see Ref. [13]. These start from a local vertex that encodes all DMFT correlations and subsequently generates nonlocal correlations through the Bethe-Salpeter equation or parquet equations. Quite naturally these extensions allow for a better description of two-particle quantities such as the (quantum) critical behavior in the vicinity of a phase transition [14–17], spin-fluctuation-induced pseudogaps [18–20], and superconducting instabilities [21,22].

The next level, the three-particle Green's function and vertices, are hitherto by-and-large a blank spot in our understanding of strongly correlated electron systems. First results for the diagrammatic extensions of DMFT [23] show that three-particle vertices are, at least in some parameter regimes of the Hubbard model, relevant. While our physical understanding and intuition is presently much more based on the one- and two-particle physics, there are also physical processes that are generically connected to three-particle correlators:

Take for example Raman scattering, with an incoming and outgoing light frequency and a transferred phonon frequency. These three bosonic frequencies are connected to three electrons (particles), each with one creation and one annihilation operator. The same applies to the Hall response, i.e., the off-diagonal conductivity in a magnetic field. The conductivity by itself is a two-particle correlator in the Kubo formalism of linear response [24]. Considering small magnetic fields, these can be treated in linear response as well, making the Hall coefficient a three-particle correlator altogether. In principle, calculating these observables requires the calculation of the full three-particle correlator. But hitherto either only a bare bubblelike diagram is taken, or corrections based on the two-particle vertex are included; see, e.g., [25–27].

Another research area that is the domain of correlators with more than two particles is nonlinear response [24,28]. These responses are in general weaker than linear responses and often the most relevant correction is thus the second-order response that is connected to a three-particle correlator. Interestingly, Refs. [29,30] found that correlation effects can enhance nonlinear responses in strongly correlated electron systems, but again they only took into account one-particle renormalizations; full vertex corrections were still neglected.

Three-particle correlators are also employed for calculating two-particle correlators reliably using the so-called improved estimators based on the equation of motion [31–35].

Against this background, it is the aim of the present paper to do some first steps in computing, analyzing, and understanding these three-particle correlators. Specifically, we consider correlators of three bosonic operators and thus three time arguments (or two time differences or frequencies). For the sake of simplicity, and to keep the numerical effort manageable, we concentrate on local correlators of an Anderson impurity model (including one at DMFT self-consistency for the two-dimensional Hubbard model). Since the Raman and

Hall response couple to light through nonlocal fermionic operators, we focus here on the nonlinear response described by local operators only. There are just three local nonvanishing three-particle correlators (and symmetrically related ones): a second-order density susceptibility (*nnn*) with three density operators, a mixed density-magnetic susceptibility (*nzz*) describing the second-order response of the density to a magnetic field in the *z* direction, and a chiral susceptibility (*xyz*). The latter corresponds to a correlator with one spin in all three directions. These are arranged like the thumb, index, and middle finger of the right hand and hence chiral according to the definition introduced by Kelvin in 1884 [36] (not invariant under any mirror transformation). Such a chiral susceptibility arises in the continuity equation of the *t*-*J* model or in the presence of the direct exchange interaction [37].

The outline of the paper is as follows: In Sec. II we give a very brief introduction to response theory and define all necessary two- and three-particle quantities as well as the relationships between them and the response functions. Section III describes the models we use in our calculations and why we chose them. The numerical results are then presented and analyzed in Sec. IV. Finally, in Secs. V and VI we give a conclusion and outlook.

II. THEORY

In general, response theory describes the relation between cause and effect. For our purposes, this boils down to quantifying how the expectation value of an arbitrary, bosonic operator $\langle \hat{A}_i \rangle$ depends on some external "force" F_j. As shown in detail in Appendix A, this can be studied by expanding $\langle \hat{A}_i \rangle$ in a functional Taylor series:

$$\langle \hat{A}_i(\tau) \rangle_{\mathbf{F}} = \langle \hat{A}_i(\tau) \rangle_{\mathbf{F}=0} + \sum_j \int_0^\beta d\tau' F_j(\tau') \chi_{ji}^{(1)}(\tau', \tau)$$
$$+ \frac{1}{2} \sum_{jk} \int_0^\beta \int_0^\beta d\tau' d\tau'' F_j(\tau') F_k(\tau'')$$
$$\times \chi_{jki}^{(2)}(\tau', \tau'', \tau) + \cdots . \quad (1)$$

Here, we express everything in imaginary time τ, which runs from zero to $\beta = 1/T$, the inverse temperature. We call the expansion coefficients $\chi^{(1)}$ and $\chi^{(2)}$ the first-order or linear, and the second-order or nonlinear response function, respectively. They are simply functional derivatives of $\langle \hat{A}_i \rangle$ with respect to F_j, and according to Eqs. (A15) and (A16) they read

$$\chi_{ij}^{(1)}(\tau, \tau') = \frac{\delta}{\delta F_i(\tau)} \langle \hat{A}_j(\tau') \rangle \Big|_{\mathbf{F}=0}$$
$$= \langle \mathrm{T} \hat{A}_i(\tau) \hat{A}_j(\tau') \rangle - \langle \hat{A}_i \rangle \langle \hat{A}_j \rangle \quad (2)$$

for the first order, and

$$\chi_{ijk}^{(2)}(\tau, \tau', \tau'') = \frac{\delta}{\delta F_i(\tau)} \frac{\delta}{\delta F_j(\tau')} \langle \hat{A}_k(\tau'') \rangle \Big|_{\mathbf{F}=0}$$
$$= \langle T \hat{A}_i(\tau) \hat{A}_j(\tau') \hat{A}_k(\tau'') \rangle$$
$$- \langle \hat{A}_i \rangle \chi_{jk}(\tau', \tau'') - \langle \hat{A}_j \rangle \chi_{ik}(\tau, \tau'')$$
$$- \langle \hat{A}_k \rangle \chi_{ij}(\tau, \tau') - \langle \hat{A}_i \rangle \langle \hat{A}_j \rangle \langle \hat{A}_k \rangle \quad (3)$$

for the second order. Here, T is the time ordering operator and $\hat{A}_i$ are the bosonic operators that the external fields F_i couple to, i.e., the Hamiltonian contains a perturbation term of the form $-\sum_i \hat{A}_i F_i$. If not indicated otherwise, the expectation values are computed with respect to the unperturbed Hamiltonian. From now on, we also drop the superscript denoting the order of the response function whenever the (number of) arguments allow us to infer it.

In Matsubara space, the linear response function reads

$$\chi_{ij}^\omega = \int_0^\beta \chi_{ij}(\tau) e^{i\omega\tau} d\tau$$
$$= \langle T \hat{A}_i(\tau) \hat{A}_j \rangle^\omega - \delta_{\omega 0} \beta \langle \hat{A}_i \rangle \langle \hat{A}_j \rangle, \quad (4)$$

while the nonlinear response function is given by

$$\chi_{ijk}^{\omega_1 \omega_2} = \int_0^\beta \int_0^\beta \chi_{ijk}(\tau_1, \tau_2) e^{i(\omega_1 \tau_1 + \omega_2 \tau_2)} d\tau_1 d\tau_2$$
$$= \langle T \hat{A}_i(\tau_1) \hat{A}_j(\tau_2) \hat{A}_k \rangle^{\omega_1 \omega_2} - \delta_{\omega_1 0} \beta \langle \hat{A}_i \rangle \chi_{jk}^{\omega_2}$$
$$- \delta_{\omega_2 0} \beta \langle \hat{A}_j \rangle \chi_{ik}^{\omega_3} - \delta_{\omega_3 0} \beta \langle \hat{A}_k \rangle \chi_{ij}^{\omega_1}$$
$$- \delta_{\omega_1 0} \delta_{\omega_2 0} \beta^2 \langle \hat{A}_i \rangle \langle \hat{A}_j \rangle \langle \hat{A}_k \rangle. \quad (5)$$

Here, we use time-translation invariance to effectively get rid of one imaginary-time argument, $\omega_3 = -\omega_1 - \omega_2$, and the frequency superscript for the expectation values indicates the Fourier transform of the corresponding imaginary-time expressions defined in Eqs. (2) and (3).

We see that the response functions are nothing but two- and three-particle correlators minus their disconnected terms.

So far everything is formulated with general, bosonic operators $\hat{A}_i$. For the rest of this paper, however, we are only interested in the cases in which those are density and spin operators:

$$\hat{n} = \hat{n}_\uparrow + \hat{n}_\downarrow = \hat{c}_\uparrow^\dagger \hat{c}_\uparrow + \hat{c}_\downarrow^\dagger \hat{c}_\downarrow, \quad (6)$$

$$\hat{\sigma}_i = \begin{pmatrix} \hat{c}_\uparrow^\dagger & \hat{c}_\downarrow^\dagger \end{pmatrix} \underline{\underline{\sigma}}_i \begin{pmatrix} \hat{c}_\uparrow \\ \hat{c}_\downarrow \end{pmatrix} \quad (7)$$

with fermionic creation and annihilation operators $\hat{c}^\dagger$ and $\hat{c}$ as well as Pauli matrices $\underline{\underline{\sigma}}_i$. In the Hamiltonian they couple as $\epsilon \hat{n}$ and $-\mathbf{h}\hat{\sigma}$ to (the change of) the one-particle energy ϵ and magnetic field $\mathbf{h}$.

Let us further introduce the following compact notation for the full, bosonic, two-particle, density, and spin correlators:

$$X_{\sigma_1, \dots, \sigma_4}(\tau) = \langle T \hat{c}_{\sigma_1}^\dagger(\tau^+) \hat{c}_{\sigma_2}(\tau) \hat{c}_{\sigma_3}^\dagger(0^+) \hat{c}_{\sigma_4}(0) \rangle, \quad (8)$$

$$X_{\alpha\beta} = \sum_{\sigma_1, \dots, \sigma_4} s_\alpha^{\sigma_1 \sigma_2} s_\beta^{\sigma_3 \sigma_4} X_{\sigma_1, \dots, \sigma_4}, \quad (9)$$

$$\underline{\underline{s}}_\alpha = \begin{cases} \mathbb{1}, & \alpha = n, \\ \underline{\underline{\sigma}}_\alpha, & \alpha \in \{x, y, z\}, \end{cases} \quad (10)$$

where $\tau^+ = \lim_{\varepsilon \to 0} \tau + \varepsilon$ and $0^+ = \lim_{\varepsilon \to 0} 0 + \varepsilon$. Analogously, on the three-particle level we define

$$X_{\sigma_1, \dots, \sigma_6}(\tau_1, \tau_2)$$
$$= \langle T \hat{c}_{\sigma_1}^\dagger(\tau_1^+) \hat{c}_{\sigma_2}(\tau_1) \hat{c}_{\sigma_3}^\dagger(\tau_2^+) \hat{c}_{\sigma_4}(\tau_2) \hat{c}_{\sigma_5}^\dagger(0^+) \hat{c}_{\sigma_6}(0) \rangle, \quad (11)$$

$$X_{\alpha\beta\gamma} = \sum_{\sigma_1, \dots, \sigma_6} s_\alpha^{\sigma_1 \sigma_2} s_\beta^{\sigma_3 \sigma_4} s_\gamma^{\sigma_5 \sigma_6} X_{\sigma_1, \dots, \sigma_6}. \quad (12)$$

In this notation, the response functions read

$$\chi_{\alpha\beta} = \mathrm{conn}\, X_{\alpha\beta}, \quad \chi_{\alpha\beta\gamma} = \mathrm{conn}\, X_{\alpha\beta\gamma}, \quad (13)$$

where conn denotes only fully connected terms.

On the two-particle level, only the response of the density to changes of the one-particle energy, χ_d, and the response of the magnetization to changes of the magnetic field in the same direction, χ_m, do not vanish:[1]

$$\chi_d(\tau) = -\frac{\delta\langle\hat{n}\rangle}{\delta\epsilon(\tau)} = \chi_{nn}(\tau), \quad (14)$$

$$\chi_m(\tau) = \frac{\delta\langle\hat{\sigma}_i\rangle}{\delta h_i(\tau)} = \chi_{ii}(\tau) \text{ with } i = x, y, z. \quad (15)$$

Using Eqs. (2), (8), and (9), we can derive well-known relations for the linear response functions:

$$\chi_{nn}(\tau) = X_{nn}(\tau) - \langle\hat{n}\rangle^2 = 2[\chi_{\uparrow\uparrow}(\tau) + \chi_{\uparrow\downarrow}(\tau)], \quad (16)$$

$$\chi_{zz}(\tau) = X_{zz}(\tau) = 2[\chi_{\uparrow\uparrow}(\tau) - \chi_{\uparrow\downarrow}(\tau)], \quad (17)$$

where the spin susceptibilities are $\chi_{\sigma\sigma'} = -\delta\langle\hat{n}_{\sigma'}\rangle/\delta\epsilon_\sigma$ with ϵ_σ denoting the (change of) the one-particle energy for spin σ only, and we assume SU(2) symmetry.

On the three-particle level, only the following response functions do not vanish:[2]

$$\chi_{nnn}(\tau_1, \tau_2) = \frac{\delta}{\delta\epsilon(\tau_1)} \frac{\delta\langle\hat{n}\rangle}{\delta\epsilon(\tau_2)} = \frac{\delta\chi_d(\tau_2)}{\delta\epsilon(\tau_1)}, \quad (18)$$

$$\chi_{nzz}(\tau_1, \tau_2) = \chi_{nxx}(\tau_1, \tau_2) = \chi_{nyy}(\tau_1, \tau_2)$$
$$= -\frac{\delta}{\delta\epsilon(\tau_1)} \frac{\delta\langle\hat{\sigma}_i\rangle}{\delta h_i(\tau_2)} = -\frac{\delta\chi_m(\tau_2)}{\delta\epsilon(\tau_1)}, \quad (19)$$

$$\chi_{xyz}(\tau_1, \tau_2) = \frac{\delta}{\delta h_x(\tau_1)} \frac{\delta\langle\hat{\sigma}_z\rangle}{\delta h_y(\tau_2)}. \quad (20)$$

We call them the second-order density, density-magnetic, and chiral response functions, respectively. In Appendix B we derive relations similar to Eqs. (16) and (17) for them. They show, e.g., that X_{xyz} contains no disconnected terms that need to be subtracted—just like X_{zz} on the two-particle level. Furthermore, in the special case of half-filling, i.e., $n_\sigma = 1/2 = 1 - n_\sigma$, we show that χ_{nnn} and χ_{nzz} vanish.

Remembering the usual definition of an n-particle Green's function,

$$G^n_{\sigma_1\sigma_2...\sigma_{2n}}(\tau_1, \tau_2, \ldots, \tau_{2n})$$
$$= (-1)^n \langle T\hat{c}_{\sigma_1}(\tau_1)\hat{c}^\dagger_{\sigma_2}(\tau_2) \cdots \hat{c}^\dagger_{\sigma_{2n}}(\tau_{2n})\rangle, \quad (21)$$

and looking at Eqs. (8)–(13), we see that the response functions are basically given by the connected parts of equal-time Green's functions. We only have to take care of the different order of creation and annihilation operators,

$$X_{\sigma_1,...,\sigma_4}(\tau) = G^2_{\sigma_2\sigma_1\sigma_4\sigma_3}(\tau, \tau^+, 0, 0^+), \quad (22)$$

---

[1] The extra minus in Eq. (14) is necessary because the density couples with $+\epsilon\hat{n}$, and a derivative with respect to ϵ brings down $-\hat{n}$ (see Appendix A), but according to Eq. (13) we want $\chi_d = \chi_{nn} = +\mathrm{conn}\langle T\hat{n}\hat{n}\rangle$.

[2] The extra minus in Eq. (19) is there for the same reason as in Eq. (14).
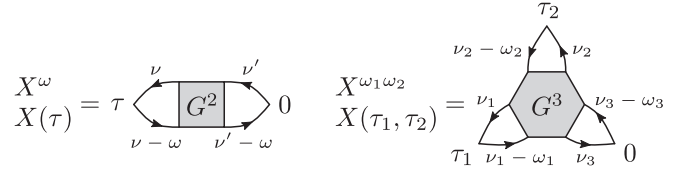

FIG. 1. Diagrammatic representation of the full two- and three-particle correlators. For brevity, the time and frequency labels are given in the same diagrams.

$$X_{\sigma_1,...,\sigma_6}(\tau_1, \tau_2) = G^3_{\sigma_2\sigma_1\sigma_6\sigma_5\sigma_4\sigma_3}(\tau_1, \tau_1^+, 0, 0^+, \tau_2, \tau_2^+). \quad (23)$$

Let us finally also define the Fourier transform,

$$X^{\omega_1\omega_2}_{\sigma_1,...,\sigma_6} = \int_0^\beta \int_0^\beta X_{\sigma_1,...,\sigma_6}(\tau_1, \tau_2) e^{i\omega_1\tau_1 + i\omega_2\tau_2} d\tau_1 d\tau_2, \quad (24)$$

where ω_1 and ω_2 are bosonic Matsubara frequencies.

With this we can give a diagrammatic representation of the correlators and response functions. Figure 1 shows the diagrams for the full two- and three-particle correlators with time and frequency labels. A particle-hole notation is chosen for the latter. (See Appendix C for a detailed look at all 15 frequency notations of the three-particle Green's function.)

To get a diagrammatic representation of the response functions, we do a decomposition of the full correlators and therefore Green's functions. Details for the three-particle case can be found in Appendix D. The diagrammatic results are shown in Fig. 2. Here we see that the terms in Eqs. (2)–(5), which we already called disconnected, are in fact represented by disjoint diagrams. Figure 2 further decomposes the connected diagrams of $\chi^{(1)}$ and $\chi^{(2)}$ and introduces the bare or bubble terms χ_0, which only contain Green's functions, the first-order terms $\chi_1^{(2)}$, which are three-particle diagrams with a single two-particle vertex F, and χ_{vertex}, which contains corrections from the "largest" possible vertex. When studying the results in Sec. IV, we are especially interested in $\chi_{\mathrm{vertex}}^{(2)}$ since it contains diagrams where all three particles interact with each other.

III. MODELS

For simplicity, we mainly employ the Anderson impurity model, but some results for the Hubbard model as well as for the atomic limit, which is the same for both, are also shown. The results for these three cases are presented in the corresponding subsections of Sec. IV.

A. Atomic limit

As a simple toy model, we consider the atomic limit with Hamiltonian $\hat{H}_{\mathrm{AL}} = \epsilon(\hat{n}_\uparrow + \hat{n}_\downarrow) - h(\hat{n}_\uparrow - \hat{n}_\downarrow) + U\hat{n}_\uparrow\hat{n}_\downarrow$, where $\epsilon = -U/2$ and h is a magnetic field. This model can be solved exactly using the Lehmann representation.

B. Anderson impurity model

We use the Anderson impurity model (AIM) with (i) a single bath site and (ii) a constant density of states (DOS). The former is chosen because it can easily be solved with
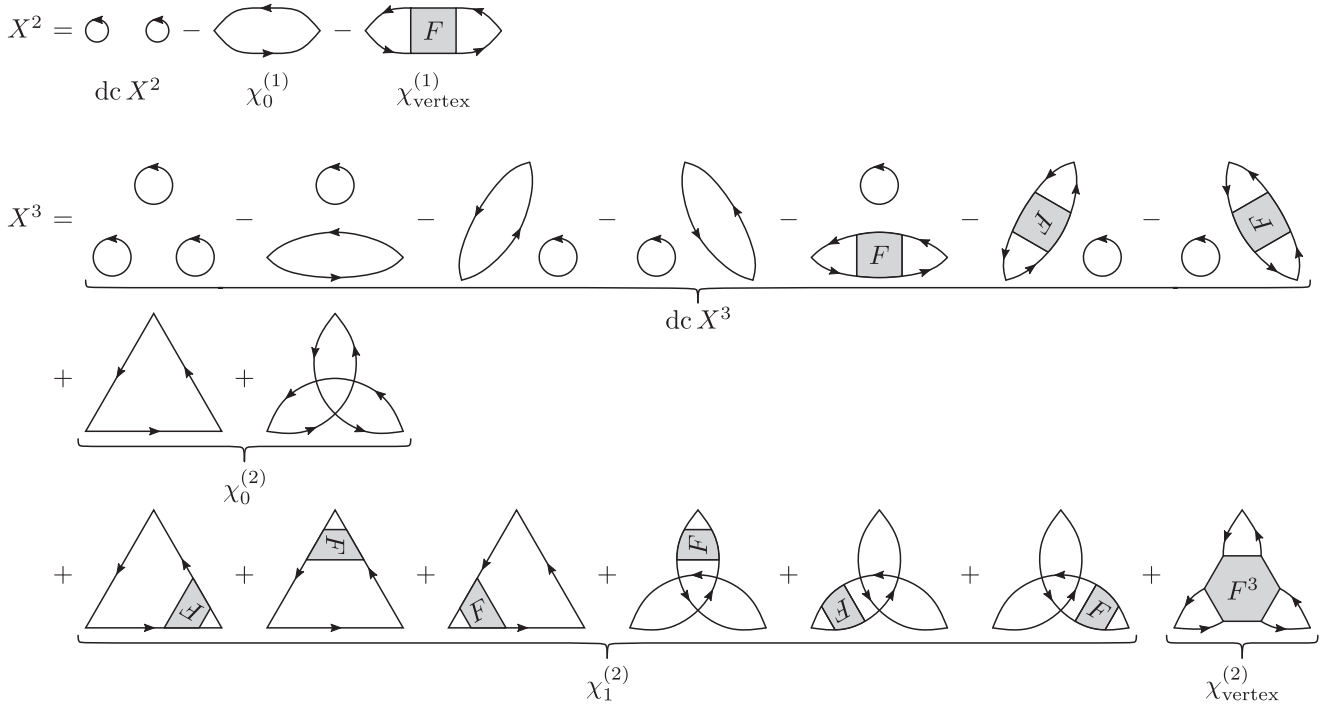
FIG. 2. Diagrammatic representation of the decomposition of the full, two-, and three-particle correlators X into disconnected terms $\mathrm{dc}\,X$, bare or bubble terms χ_0, first-order terms χ_1, and full vertex terms χ_{vertex}. Time and frequency labels are omitted to avoid clutter. They can easily be inferred from Fig. 1.

exact diagonalization and therefore serves as a test for the implementation of the three-particle calculations. The latter is used for most other results because, while still relatively simple and therefore fast to solve on modern computers, it already shows the effects of strong electronic correlation. The low computational complexity of the model, is important because of two things: First, we expect that the search for regions where three-particle effects are relevant involves sampling a potentially large amount of points in the phase diagram. Second, we solve the AIM by means of a quantum Monte Carlo (QMC) solver. Once the interesting points are found, getting accurate, low-noise results for $\chi^{(2)}$ can require a lot of QMC samples since the disconnected parts that have to be subtracted first (see Sec. II) potentially make up most of the correlation function.

The Hamiltonian for the AIM is in general given by

$$\hat{H}_{\mathrm{AIM}} = \epsilon \hat{n} + U \hat{n}_\uparrow \hat{n}_\downarrow + \sum_{k,\sigma} \epsilon_k \hat{c}^\dagger_{k\sigma} \hat{c}_{k\sigma}$$
$$+ \sum_{k,\sigma} (V_k \hat{f}^\dagger_\sigma \hat{c}_{k\sigma} + V^*_k \hat{c}^\dagger_{k\sigma} \hat{f}_\sigma), \qquad (25)$$

where ϵ, $\hat{f}^\dagger_\sigma$, and $\hat{f}_\sigma$ are the energy level as well as the creation and annihilation operator of the impurity, $\hat{n}_\sigma = \hat{f}^\dagger_\sigma \hat{f}_\sigma$ is the impurity density operator for spin σ, $\hat{n} = \hat{n}_\uparrow + \hat{n}_\downarrow$ is the total density operator for the impurity, U is the on-site Coulomb interaction, ϵ_k, $\hat{c}^\dagger_{k,\sigma}$, and $\hat{c}_{k\sigma}$ are the energy levels as well as creation and annihilation operators for the bath, and V is the hybridization.

In the simplest case of only a single bath site, we have $\epsilon_{k=1} = \epsilon_1$. The second case we consider has a constant DOS,

$$\rho(\epsilon) = \begin{cases} \rho_0, & -D \leqslant \epsilon \leqslant D, \\ 0 & \text{otherwise} \end{cases} \qquad (26)$$

and a real hybridization $V_k \equiv V$. This means that there is a continuous set of bath sites with energies between $-D$ and D.

C. Hubbard model

The Hubbard model is one of the standard models when it comes to investigating strong electronic correlations, but it is more difficult to solve than the AIM. For our calculations, we choose the single-band square-lattice Hubbard model, which is defined by the following Hamiltonian:

$$\hat{H}_{\mathrm{HM}} = -t \sum_{\langle ij \rangle, \sigma} (\hat{c}^\dagger_{i\sigma} \hat{c}_{j\sigma} + \hat{c}^\dagger_{j\sigma} \hat{c}_{i\sigma}) + U \sum_i \hat{n}_{i\uparrow} \hat{n}_{i\downarrow}. \qquad (27)$$

As usual, t is the hopping integral, $\sum_{\langle ij \rangle}$ denotes the sum over nearest neighbors, $\hat{c}^\dagger_{i\sigma}$ and $\hat{c}_{i\sigma}$ are the creation and annihilation operators for electrons with spin σ at site i, U is the on-site interaction strength, and $\hat{n}_{i\sigma} = \hat{c}^\dagger_{i\sigma} \hat{c}_{i\sigma}$ is the density operator for electrons with spin σ at site i.

Since the Hubbard model cannot be solved, also not numerically, except for very small clusters, we employ DMFT [2–5] for an approximate solution. DMFT actually maps the Hubbard model onto a self-consistent solution of the AIM. The susceptibilities that we calculate here are local impurity susceptibilities only. This means that these susceptibilities are actually also obtained from the AIM, but now at DMFT

self-consistency. They differ from the lattice susceptibilities, also the local ones, since the applied fields can also affect the DMFT bath of the auxiliary Anderson model. This effect is not taken into account here.

IV. RESULTS

The numerical results in this section are obtained with `w2dynamics` [38], a continuous-time quantum Monte Carlo (CT-QMC) solver using the hybridization expansion [39]. Only for the AIM with one bath site do we also employ exact diagonalization (ED). Furthermore, let us mention that a numerical renormalization group (NRG) has been successfully employed recently for calculating multipoint correlators of the AIM [40]. Postprocessing of the CT-QMC results is done with the Python package `w2diag` [41] written to, among other things, implement the equations in Sec. II and compute the first- and second-order susceptibilities $\chi^{(1)}$ and $\chi^{(2)}$, involving two- and three-particle correlators, respectively.

The results for the atomic limit are computed analytically through the Lehmann representation.

A dataset containing all numerical data and plot scripts used to generate the figures in this section is publicly available on the TU Wien Research Data repository [42]. The dataset also contains auxiliary data files, parameter files, and submission scripts for better reproducibility.

A. Atomic limit

In the atomic limit, we only have four states: empty site, single occupation with spin $\sigma \uparrow$ or $\downarrow$, and double occupation with energies zero, $\epsilon \mp h$, and $2\epsilon + U$, respectively. We calculate the three-particle correlators of the atomic limit, as defined in Eqs. (11), (12), and (24), employing the Lehmann representation in Appendix F. As shown in Appendix G, with SU(2) symmetry and swapping relations we only obtain three independent flavor combinations, $\alpha\beta\gamma = nnn, nzz, xyz$, for the second-order (three-operator) susceptibility. Moreover, the first two flavor combinations correspond, in the atomic limit, to conserved and mutually commuting operators. As a result, these three-particle correlators are purely thermal: $X_{nnn}^{\omega_1\omega_2} = X_{nnn}\delta_{\omega_1 0}\delta_{\omega_2 0}$, $X_{nzz}^{\omega_1\omega_2} = X_{nzz}\delta_{\omega_1 0}\delta_{\omega_2 0}$. Only $X_{xyz}^{\omega_1\omega_2}$ has a frequency structure.

Let us first consider the noninteracting case ($U = 0$) at half-filling ($\epsilon = 0$), without a magnetic field ($h = 0$). We evaluate the three-particle correlator using Wick's theorem:

$$
\begin{aligned}
X_{\sigma_1,\dots,\sigma_6}^{\omega_1\omega_2} = {} & \beta^2 \langle \hat{n}_{\sigma_1} \rangle \langle \hat{n}_{\sigma_2} \rangle \langle \hat{n}_{\sigma_3} \rangle \, \delta_{\sigma_1\sigma_1'}\delta_{\sigma_2\sigma_2'}\delta_{\sigma_3\sigma_3'}\delta_{\omega_1 0}\delta_{\omega_2 0} \\
& - \beta\langle \hat{n}_{\sigma_1} \rangle \frac{1}{\beta} \sum_\nu G_{\sigma_2}^\nu G_{\sigma_3}^{\nu+\omega} \delta_{\sigma_1\sigma_1'}\delta_{\sigma_2\sigma_3'}\delta_{\sigma_3\sigma_2'}\delta_{\omega_1 0} \\
& - \beta\langle \hat{n}_{\sigma_2} \rangle \frac{1}{\beta} \sum_\nu G_{\sigma_1}^\nu G_{\sigma_3}^{\nu+\omega} \delta_{\sigma_1\sigma_3'}\delta_{\sigma_2\sigma_2'}\delta_{\sigma_3\sigma_1'}\delta_{\omega_2 0} \\
& - \beta\langle \hat{n}_{\sigma_3} \rangle \frac{1}{\beta} \sum_\nu G_{\sigma_1}^\nu G_{\sigma_2}^{\nu+\omega} \delta_{\sigma_1\sigma_2'}\delta_{\sigma_2\sigma_1'}\delta_{\sigma_3\sigma_3'}\delta_{\omega_1,-\omega_2} \\
& + \frac{1}{\beta} \sum_\nu G_{\sigma_1}^\nu G_{\sigma_2}^{\nu+\omega_1} G_{\sigma_3}^{\nu+\omega_1+\omega_2} \\
& + \frac{1}{\beta} \sum_\nu G_{\sigma_2}^\nu G_{\sigma_1}^{\nu+\omega_2} G_{\sigma_3}^{\nu+\omega_1+\omega_2}. \qquad (28)
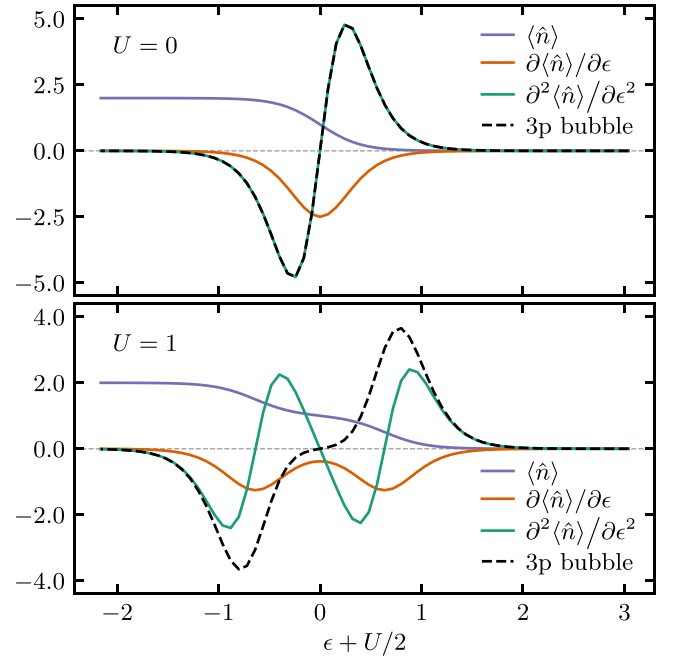\end{aligned}
$$

FIG. 3. Density $\langle \hat{n} \rangle$ as a function of the energy ϵ (purple) in the atomic limit ($\beta = 5$, $h = 0$). Orange and green curves show the first and second derivative, respectively; a black dashed line shows the three-particle bubble. Top panel: noninteracting limit. Bottom panel: $U = 1$.

The first term with three densities n corresponds to the fully disconnected, first diagram for X^3 in Fig. 2. The terms two to four have one density and a bare bubble susceptibility (for $U = 0$: $\chi_d = \chi_m = -\frac{1}{\beta}\sum_\nu G^\nu G^{\nu+\omega}$), as the next three diagrams for X^3 in Fig. 2. All of these terms are disconnected and do not contribute to the second-order, three-particle susceptibility.

The last two terms in Eq. (28) are the bare bubble second-order susceptibility $\chi_0^{(2)}$, represented diagrammatically in the second line of diagrams for X^3 in Fig. 2 [cf. Eqs. (18)–(20)]. This connected part contains the essential three-particle information. While for $U = 0$ it is given through the (two) bare bubble diagrams, vertex corrections become important for $U \neq 0$. Namely, there are corrections with the two-particle vertex F connecting two Green's function lines as well as more complicated three-particle vertex corrections with F^3. The latter connects all three Green's function lines of the bubble through interactions.

As a technical note: In Eq. (28) the connected part appears next to the disconnected term of order β^2. Therefore, a stochastic measurement of the three-particle susceptibility has a less favorable signal-to-noise ratio at low temperatures than the two-particle one, whose disconnected term is only of order β.

The upper panel of Fig. 3 shows the density $\langle \hat{n} \rangle$ of the noninteracting system as a function of the energy ϵ ($\beta = 5$), together with its first and second derivatives with respect to ϵ. The latter is computed from Eq. (5), but with partial instead of functional derivatives and therefore static correlators,
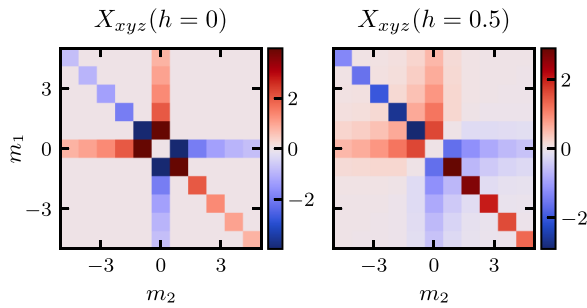
FIG. 4. Full three-particle correlator with flavors x, y, z drawn as a function of the two indices $m_{i=1,2}$ of the bosonic Matsubara frequencies $\omega_i = m_i 2\pi T$; $U = \epsilon = 0$, $\beta = 5$. In the atomic limit, only this flavor combination retains a frequency structure due to noncommutativity of the spin operators. Left: no magnetic field. Right: magnetic field in the z-direction, $h = 0.5$.

yielding

$$\frac{\partial^2 \langle \hat{n} \rangle}{\partial \epsilon^2} = X_{nnn}^{00} + 3\beta \langle \hat{n} \rangle \frac{\partial \langle \hat{n} \rangle}{\partial \epsilon} - \beta^2 \langle \hat{n} \rangle \langle \hat{n} \rangle \langle \hat{n} \rangle, \qquad (29)$$

where $\partial \langle \hat{n} \rangle / \partial \epsilon = -X_{nn}^0 + \beta \langle \hat{n} \rangle \langle \hat{n} \rangle$ [cf. Eq. (14)] and $\langle \hat{n} \rangle$ are computed in the usual way; see, e.g., Ref. [43]. We verified that Eq. (29) coincides with the analytical and numerical second derivative of $\langle \hat{n} \rangle$. Also drawn is the three-particle bubble (dashed), which coincides exactly with the second derivative, as expected ($U = 0$). For negative (positive) ϵ, double occupations (empty sites) are favorable. Hence, the density $\langle \hat{n} \rangle$ shows a crossover of width $1/\beta$, and the other quantities follow as derivatives.

Next, we turn on the interaction ($U = 1$), which lifts the degeneracy of the empty, singly, and doubly occupied states at $\epsilon = 0$. As a result, the derivatives of $\langle \hat{n} \rangle$ in the lower panel of Fig. 3 acquire additional minima and maxima. It is interesting to compare $\partial^2 \langle \hat{n} \rangle / \partial \epsilon^2$ to the three-particle bubble, which lacks vertex corrections. For large dopings, the two curves coincide, which can be considered as a perturbative regime where interaction effects are small. However, in the correlated regime, near half-filling the three-particle bubble fails qualitatively. In particular, it is unable to describe the curvature of $\langle \hat{n} \rangle$ for ϵ in between the Hubbard bands.

Finally, we consider the only three-particle correlation function that retains a nontrivial frequency structure in the atomic limit: the chiral susceptibility $X_{xyz}^{\omega_1 \omega_2} = \chi_{xyz}^{\omega_1 \omega_2}$. The left panel of Fig. 4 shows this function for $U = 0$, $\epsilon = 0$, $h = 0$, $\beta = 5$. This picture does not change qualitatively when U is turned on (not shown), which underlines that the frequency structure of X_{xyz} is a result of the noncommutativity of the spin operators among each other, rather than due to a specific interaction regime. Notice also that the function is singular, that is, it vanishes exactly away from the cross and diagonal structures, since each component of the spin operator is conserved. This property does not persist for a finite magnetic field $h = 0.5$ in the z direction (right panel), which softens the cross structure, since it does not commute with the x and y components of the spin operator.
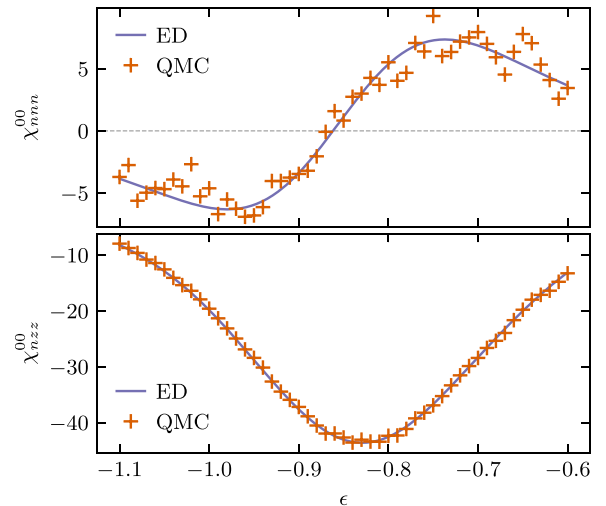

FIG. 5. Comparison of exact (ED) and stochastic (QMC) results for the AIM at $U = 1$, $\beta = 20$, hybridizing with $V = 0.2$ to a single bath site with energy $\epsilon_1 = 0.25$. The top plot shows the static, second-order, density response function χ_{nnn}^{00}, while the bottom one shows the static, second-order, density-magnetic response function χ_{nzz}^{00}.

B. AIM with one bath site

To test the correctness of the implementation of the second-order response functions in w2diag, the results are compared against solutions of an AIM with a single bath site obtained via exact diagonalization (ED). More precisely the density n and the linear, magnetic response function χ_m are computed with ED and then numerically differentiated. This yields the right-hand side of the following two formulas:

$$\chi_{nnn}^{00} = \frac{\partial^2}{\partial \epsilon^2} \langle \hat{n} \rangle, \qquad (30)$$

$$\chi_{nzz}^{00} = -\frac{\partial}{\partial \epsilon} \chi_m, \qquad (31)$$

which are basically Eqs. (18) and (19) but with partial instead of functional derivatives for denoting static response functions χ_{nnn}^{00} and χ_{nzz}^{00}. The left-hand side is computed with w2diag from QMC results obtained with w2dynamics.

The results for $U = 1$, $\beta = 20$, $V = 0.2$, and $\epsilon_1 = 0.25$ are shown as a function of ϵ in Fig. 5; those for $V = 0.05$ and $\epsilon_1 = 0$ with the same U and β are plotted in Fig. 6. We see that the agreement between stochastic and exact results is very good except for χ_{nnn} in Fig. 5 where the large noise prevents precise statements.

This trend of higher noise in the data for χ_{nnn} is something we observe in almost every computation, and it can be explained as follows: First, we measure the full three-particle correlators with similar relative noise, but since at least the static component X^{00} is usually larger in the nnn channel than in the nzz channel, the absolute error is also larger there. Second, and more importantly, when looking at Eq. (5) we see that for χ_{nnn} we have to subtract all four disconnected terms from X_{nnn}, while for χ_{nzz} three of the four terms vanish because $\langle \hat{\sigma}_z \rangle = 0$. Therefore, the magnitude of χ_{nnn}^{00} is often smaller than that of χ_{nzz}^{00}. Together this explains why the results for χ_{nnn}^{00} can have significantly higher relative noise than those
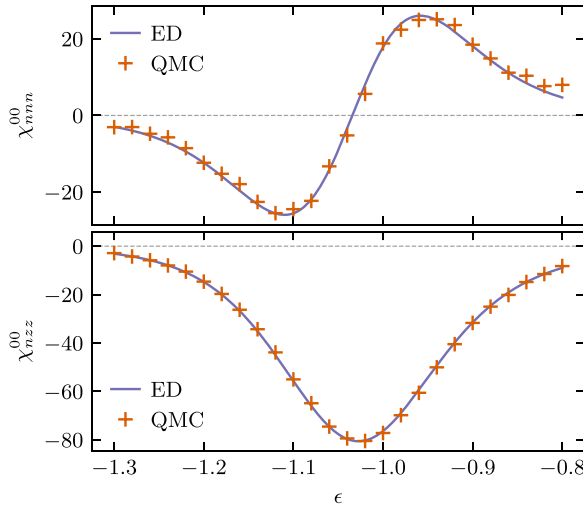
FIG. 6. Comparison of exact (ED) and stochastic (QMC) results for the AIM with a single bath site. Same as Fig. 5, but now at $U = 1$, $\beta = 20$, $V = 0.05$, and $\epsilon_1 = 0$.

for χ_{nzz}^{00}. Figure 7 in the next subsection shows this most dramatically.

C. AIM with constant DOS

To find an area with potentially large, second-order effects, we do calculations at two to five times the Kondo temperature and make an ϵ-scan starting from $-U/2$ going to smaller values. The idea behind this is to find larger nonlinear dynamics; and, going away from particle-hole symmetry $\epsilon = -U/2$ reduces the Kondo temperature so that the derivative with respect to ϵ should be sizable.

The chosen parameters are $D = 10$, $U = 6$, $V = 2$, and $\beta = 18$. They satisfy $D > U \gtrsim V$, so according to Ref. [44]
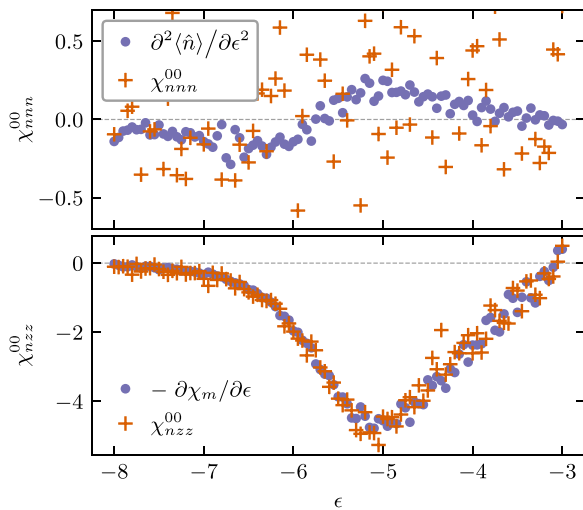

FIG. 7. Scan of $\partial^2 \langle \hat{n} \rangle / \partial \epsilon^2$, $-\partial \chi_m / \partial \epsilon$, χ_{nnn}, and χ_{nzz} vs ϵ for an AIM with constant DOS at $D = 10$, $U = 6$, $V = 2$, and $\beta = 18$. The noise of χ_{nnn} is even larger than depicted. Its data points are actually outside the plotted region and between -1.5 and 1.5. However, with that range on the y-axis the extrema of $\partial^2 \langle \hat{n} \rangle / \partial \epsilon^2$ would hardly be noticeable.
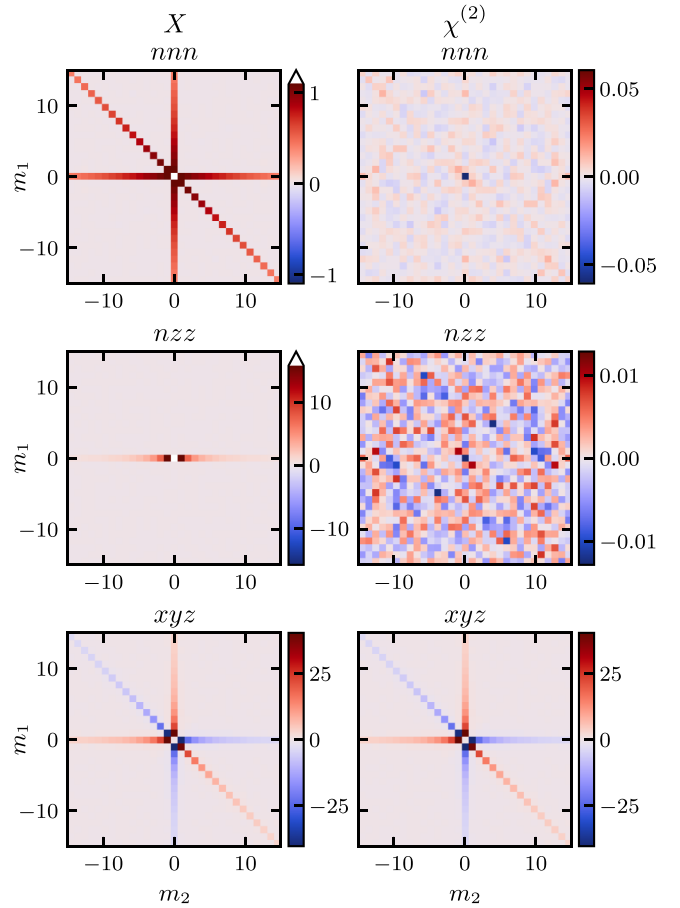

FIG. 8. Full correlation functions X (left column) and second-order response functions $\chi^{(2)}$ (right column) vs the two indices $m_{i=1,2}$ of the bosonic Matsubara frequencies $\omega_i = m_i 2\pi T$ in the density (nnn; top row), density-magnetic (nzz; center row), and chiral (xyz; bottom row) channel for an AIM with constant DOS at $D = 10$, $U = 6$, $V = 2$, $\beta = 18$ and half-filling, i.e., $\epsilon = -3$ and $n = 1$. The color bars for X_{nnn} and X_{nzz} exclude the largest value at the center because it would dominate the plots. These values are $X_{nnn}^{00} \approx 327$ and $X_{nzz}^{00} \approx 171$.

(p. 165ff) we can estimate the Kondo temperature to be $1/T_K = \beta_K \approx 64$, which means that $\beta/\beta_K \approx 3.6$.

Figure 7 shows the second derivative of the density $\partial^2 \langle \hat{n} \rangle / \partial \epsilon^2$, the first derivative of the linear, magnetic response function $\partial \chi_m / \partial \epsilon$ as well as the static, second-order, density, and density-magnetic response functions χ_{nnn}^{00} and χ_{nzz}^{00} plotted over ϵ. This time χ_{nnn}^{00} is so noisy that no useful information can be extracted (see the discussion at the end of Sec. IV B for an explanation). Nevertheless, we clearly observe the largest, second-order effects around $\epsilon = -5$ and also $\epsilon = -6.6$, so we choose those points for closer, frequency-resolved investigation.

First, however, we take a look at half-filling, i.e., $\epsilon = -U/2 = -3$ and $n = 1$. Figure 8 shows the full correlation functions $X^{\omega_1 \omega_2}$ (left column) and the second-order response functions $\chi^{\omega_1 \omega_2}$ (right column) in the density, density-magnetic, and chiral channel. The color bars for X_{nnn} and X_{nzz} exclude the largest value at the center because it would dominate the plots with values of $X_{nnn}^{00} \approx 327$ and
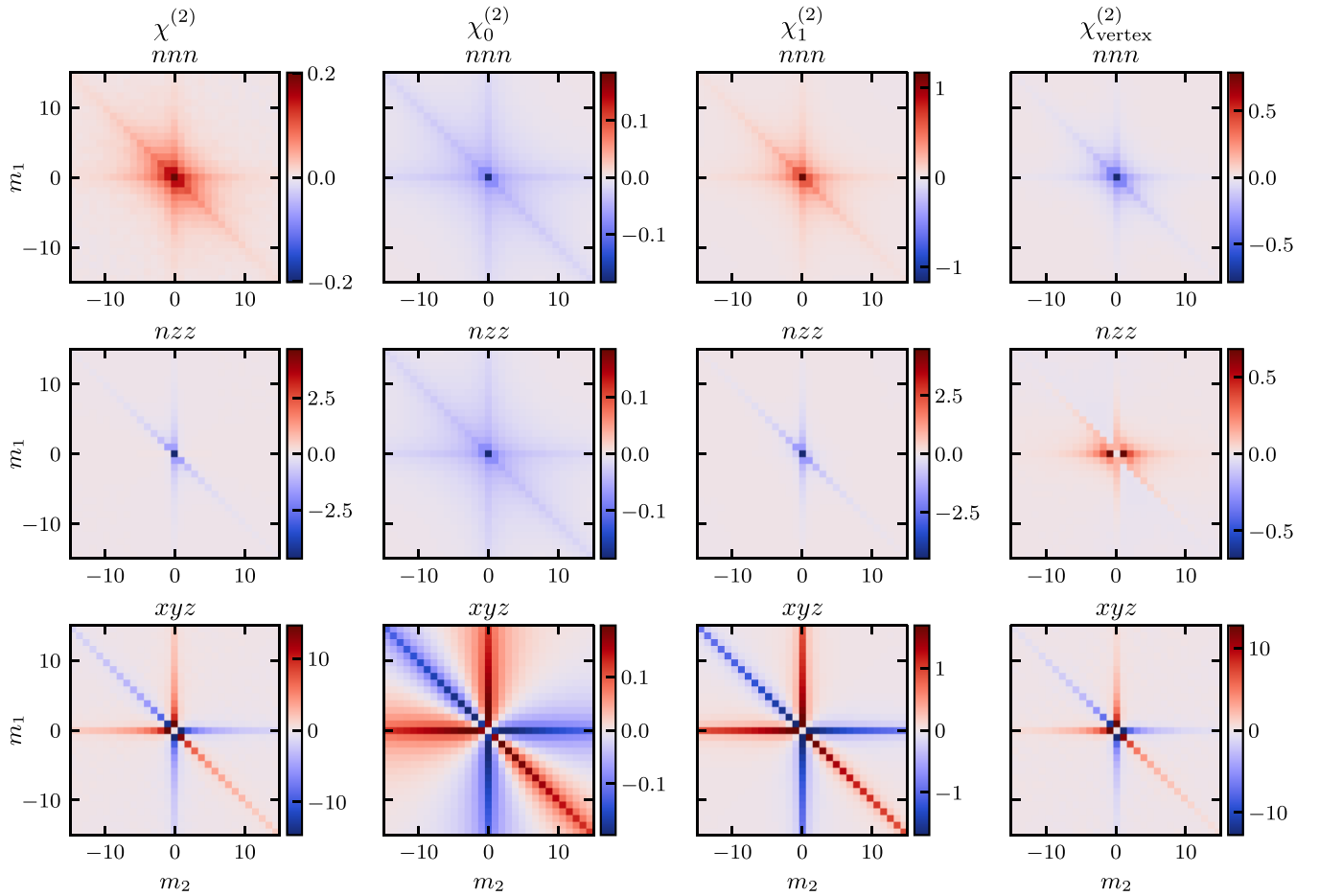
FIG. 9. Second-order response functions $\chi^{(2)}$ and their decomposition into the bubble terms $\chi_0^{(2)}$, first-order terms $\chi_1^{(2)}$, and vertex terms $\chi_{\text{vertex}}^{(2)}$ in the density (nnn), density-magnetic (nzz), and chiral (xyz) channel for an AIM with constant DOS at $D = 10$, $U = 6$, $V = 2$, $\beta = 18$, and $\epsilon = -5$ corresponding to $n \approx 1.22$.

$X_{nzz}^{00} \approx 171$. As expected from the discussion at the end of Sec. II, we see that, in this case, χ_{nnn} and χ_{nzz} vanish (the higher absolute noise at the center of χ_{nnn} comes from the large value of X_{nnn}^{00}). There is also no difference between the full correlator and the connected parts in the chiral channel. X_{nnn} and X_{nzz} clearly show the structure of the disconnected parts with their $\delta_{\omega_i 0}$ terms [see Eqs. (B12)–(B15)]. The latter are also responsible for the large values at $\omega_1 = \omega_2 = 0$ that are clipped from the color bar. Although there are no disconnected terms for X_{xyz}, it shows similar "cross" -like but antisymmetric structures. Additionally, note that in Fig. 8 we see the following order when comparing the magnitudes of the nonstatic parts: $X_{xyz} > X_{nzz} > X_{nnn}$. For the static components, this order is exactly reversed.

As discussed above, the results for the largest, second-order effects in the density and density-magnetic channel are found approximately at $\epsilon = -5$ in Fig. 7, corresponding to $n \approx 1.22$. They are shown in Fig. 9 where we plot the full, second-order response function $\chi^{(2)}$, as well as its decomposition into the bubble terms $\chi_0^{(2)}$, first-order terms $\chi_1^{(2)}$, and vertex terms $\chi_{\text{vertex}}^{(2)}$ in all three channels. For the density-like response functions, i.e., χ_{nnn} and χ_{nzz}, even after subtracting the disconnected terms we still see the maximum at the center point and "cross" -like structures along the $\omega_i = 0$

lines. Those features are, however, much less pronounced and more washed out when compared to those of X in Fig. 8. Since there are generally no disconnected terms in the chiral channel ($\chi_{xyz} = X_{xyz}$), the plot of χ_{xyz} looks almost exactly the same as before. Compared to Fig. 8, only the magnitude is reduced because of the different doping. When looking at the decomposition, the density-like channels all look rather similar and soft while the features in the chiral channel are much more pronounced and long-ranged. Regardless of that, the bubble terms $\chi_0^{(2)}$ are of similar magnitude for all channels but never a good approximation for the whole second-order response functions. They are too small and in the density channel the bubble even has the wrong sign. The first-order terms $\chi_1^{(2)}$ are larger (sometimes too large) and always have the right sign, but that is still not enough. Across all three channels the corrections from the three-particle vertex $\chi_{\text{vertex}}^{(2)}$ have sizable contributions that cannot be neglected. Especially χ_{xyz} is dominated by these terms. When comparing maximum magnitudes of the second-order response functions, we see the same ordering as for the nonstatic parts of X in the half-filled case: $\chi_{xyz} > \chi_{nzz} > \chi_{nnn}$.

Figure 10 shows the same plots as Fig. 9 but for $\epsilon = -6.6$, corresponding to $n \approx 1.68$, where the second-largest, second-order effects in the density channel are found. We see in all
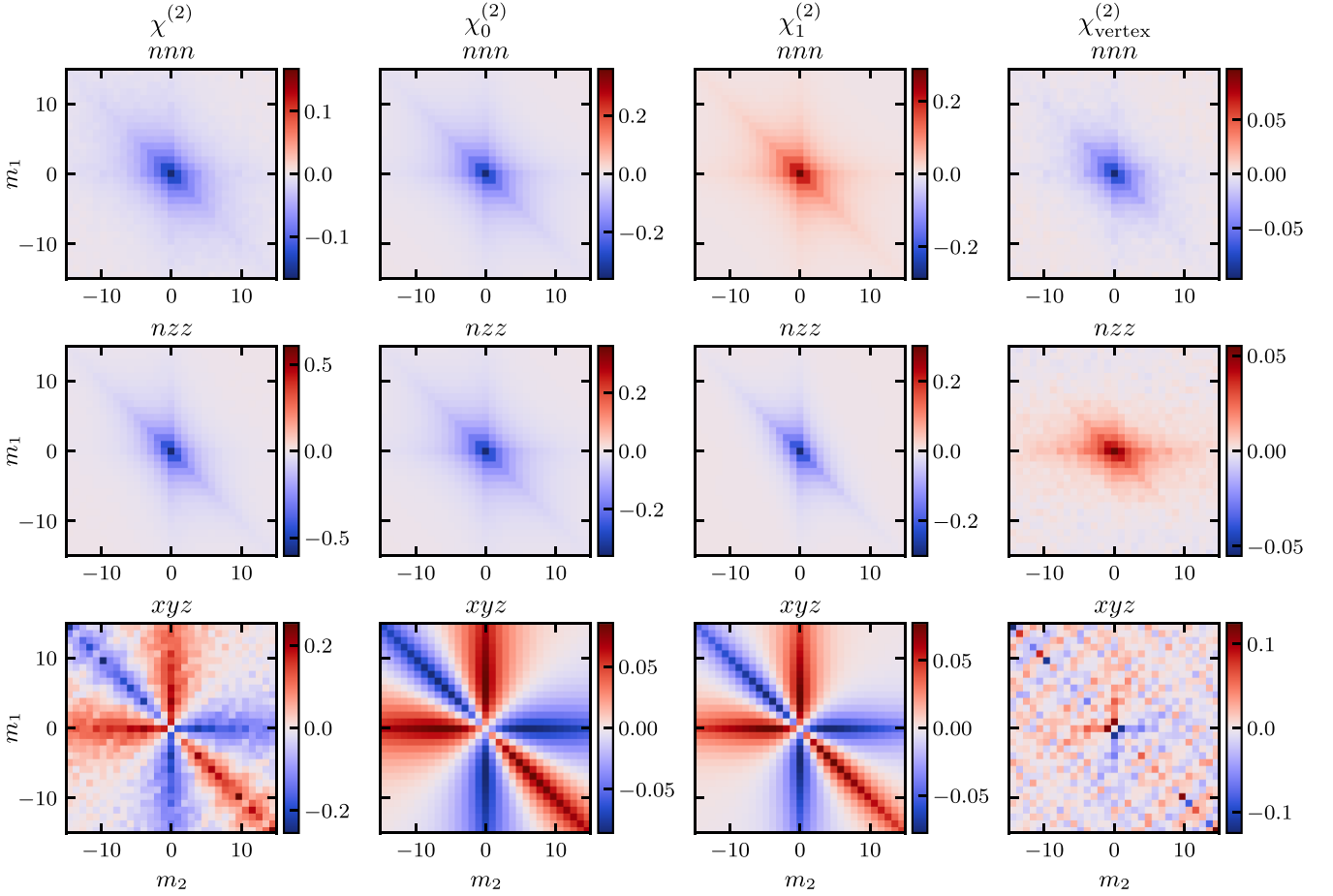
FIG. 10. Same as Fig. 9 except now $\epsilon = -6.6$ corresponding to $n \approx 1.68$.

plots that the features are much less pronounced. Especially the plots of the chiral channel are more washed out and, since the magnitude of χ_{xyz} is much lower than when closer to half-filling, noise becomes a problem, particularly for the three-particle vertex corrections. The sign change of χ_{nnn} is expected when looking at Fig. 7, and it means that the bubble now has the correct sign across all channels. In general, we see that at this higher doping the bubble becomes a better approximation while $\chi_1^{(2)}$ and $\chi_{vertex}^{(2)}$ become smaller.

Finally, we take a look at the asymptotic behavior of the second-order response functions in the limit of large Matsubara frequencies ω. More precisely we look at 1D cuts along $\omega_1 = 0$ and $\omega_2 = \omega$. From the detailed derivation in Appendix E, we get

$$\chi_{nnn}^{0\omega} \approx -\frac{1}{\omega^2} \frac{\partial \langle H_V \rangle}{\partial \epsilon}, \quad (32)$$

$$\chi_{nzz}^{0\omega} \approx -\frac{1}{\omega^2} \frac{\partial \langle H_V \rangle}{\partial \epsilon}, \quad (33)$$

$$\chi_{xyz}^{0\omega} \approx -\frac{2}{\omega} \chi_m^0, \quad (34)$$

where χ_m^0 is the static, linear magnetic response function, and H_V is the hybridization term in the Hamiltonian of the AIM

[last term in Eq. (25)]. Its derivative reads

$$-\frac{\partial}{\partial \epsilon} \langle H_V \rangle = \frac{4}{\beta} \sum_\nu \Delta_\uparrow^\nu (P_{\uparrow\uparrow}^{\nu 0} + P_{\uparrow\downarrow}^{\nu 0} + \beta(2 - \langle \hat{n} \rangle) G_\uparrow^\nu), \quad (35)$$

where Δ is the hybridization function, P is the partially contracted two-particle Green's function $P^{\nu'\omega} = \frac{1}{\beta} \sum_\nu G^{\nu\nu'\omega}$, G^ν is the one-particle Green's function, and we use SU(2) symmetry. Note that the $1/\omega$ terms for the density and density-magnetic channel vanish because they are proportional to $[\hat{n}, \hat{n}]$ and $[\hat{\sigma}_z, \hat{\sigma}_z]$, respectively.

Figure 11 compares the analytical results of Eqs. (32)–(34) with the numerical data for $\chi^{0\omega}$ at $\epsilon = -5$. The equations are multiplied with ω^2 and ω, respectively, because the tails drop so fast that a good comparison at medium to high frequencies would hardly be possible otherwise. This, however, also amplifies the noise of the numerical results. Nevertheless, we see a good agreement starting at frequencies as low as $\omega \approx 4$.

D. Hubbard model

Figure 12 shows the same plots as Figs. 9 and 10, namely the full, second-order response function $\chi^{(2)}$, the bubble terms $\chi_0^{(2)}$, the first-order terms $\chi_1^{(2)}$, and the vertex terms $\chi_{vertex}^{(2)}$ in the density, density-magnetic, and chiral channel. This time, however, they were computed for the two-dimensional
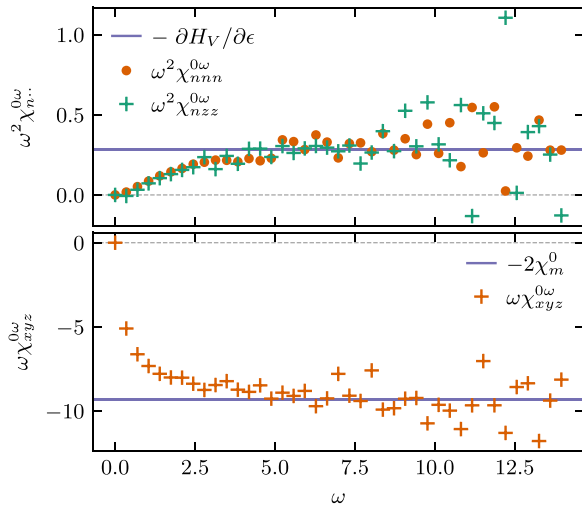
FIG. 11. Analysis of the asymptotic behavior of the second-order response functions at $\omega_1 = 0$, $\omega_2 = \omega$. The top plot shows the density and density-magnetic channel multiplied by ω^2, while in the bottom one the chiral channel is multiplied by ω. The dots and pluses represent the numerical data computed for an AIM with constant DOS at $D = 10$, $U = 6$, $V = 2$, $\beta = 18$, and $\epsilon = -5$. These are the same parameters as in Fig. 9. The solid lines are the analytically calculated asymptotic behavior taken from Eqs. (32)–(34).

Hubbard model on a square lattice with $n = 1.1$, $t = 1$ (i.e., $D = 4$), $U = 12$, and $\beta = 20$.[3] We see that for the most part the results look similar to those for the AIM with constant DOS at $\epsilon = -5$ (Fig. 9). χ_{nnn} seems even more washed out, but the biggest differences show the bubble terms of the density and density-magnetic channel, which are qualitatively different and no longer completely negative. They have a rather steep positive hill centered around $\omega_1 = \omega_2 = 0$ and a slowly decaying negative background at higher frequencies. The main takeaway that $\chi_0^{(2)}$ and $\chi_1^{(2)}$ are bad approximations is, however, still valid.

V. CONCLUSION

We have derived the equations for the frequency-resolved, nonlinear response from three-particle correlators. These are made up from three bosonic operators with three time arguments (or two time differences or frequencies). We focused here on the local correlator, the three-particle Green's function, and susceptibility ($\chi^{(2)}$) on an impurity site. However, the equations derived can be straightforwardly extended to nonlocal correlators adding a site index for each time index. We further showed how the three-particle quantities are decomposed: This involves disconnected diagrams that do not contribute to $\chi^{(2)}$ as well as two bubble diagrams $\chi_0^{(2)}$ without vertex corrections, very similar to the two-particle correlators. Then there are diagrams $\chi_1^{(2)}$ consisting of a single-particle propagator and two propagators connected by a two-particle

vertex as well as genuine three-particle vertex diagrams $\chi_{\text{vertex}}^{(2)}$ that connect all incoming and outgoing lines (cf. Fig. 2). The asymptotic behavior of the correlators is given by a $1/\omega^2$ or $1/\omega$ term, depending on whether the bosonic operators commute or not.

We have computed the correlators numerically using continuous-time QMC for the atomic limit as well as for the AIM with a single-site, a flat DOS, and at DMFT self-consistency for the two-dimensional Hubbard model. We find a sizable nonlinear density and density-magnetic response functions at high doping. At half-filling, these two nonlinear responses vanish by symmetry. The pure density (*nnn*) response function suffers from the fact that there are large contributions from disconnected terms that need to be subtracted. This leads to a rather high level of numerical noise for the actual response function. The chiral (*xyz*) response function is also sizable. It contributes at half-filling and decreases with doping. It has the largest three-particle vertex contributions. For all three nonvanishing local response functions (*nnn*, *nzz*, and *xyz*), the three-particle vertex cannot be neglected for relevant ranges of the local one-particle potential ϵ.

VI. OUTLOOK

Physically the *nnn* and *nzz* response functions can, in the case of a static third bosonic *n* operator, be related to the change of the charge susceptibility and magnetic susceptibility with respect to a change of the local one-particle potential. If the third bosonic operator becomes time- or frequency-dependent, we have the corresponding changes against a dynamic one-particle potential. The *nnn* susceptibility is therefore the second-order charge response, and *nzz* describes the nonlinear charge response to an applied magnetic field.

The chiral *xyz* susceptibility is arguably the most exotic response as there is no correspondence on the two-particle level; the *xy*, *xz*, and *yz* susceptibilities all vanish in the paramagnetic phase with SU(2) symmetry. The chiral *xyz* susceptibility describes a nonlinear response of the spin in the *x*-direction if (time-dependent) magnetic fields in both the *y*- and *z*-directions are applied. If one of the magnetic fields, say the one in the *z*-direction, is large and static, it is akin to a nuclear magnetic resonance experiment. However, here we are in second-order response, i.e., we only have a weak field in the *z*-direction. Nonetheless, there are ideas and efforts to actually measure this response function [45].

We have seen that the contribution of the three-particle vertex F^3 to the second-order susceptibility $\chi^{(2)}$ is in general not small, but comparable to (or even larger than) the bare bubble contribution $\chi_0^{(2)}$ and contributions $\chi_1^{(2)}$ from two-particle vertices plus a disconnected propagator. This means that previous approaches to calculate nonlinear responses, such as the Hall and Raman response, which only included $\chi_0^{(2)}$ or at most $\chi_1^{(2)}$, need to be reassessed for strongly correlated electron systems. Numerical approaches, as we have employed here for the local susceptibilities, become prohibitively expensive for the full lattice. This calls for developing approaches such as a three-particle Bethe-Salpeter equation for calculating the three-particle vertex F^3 also in the nonlocal case.

---

[3]Note that in this case $\chi^{(2)}$ is only the local, second-order response, as discussed above. The total one would have to include the change in the hybridization function as well.
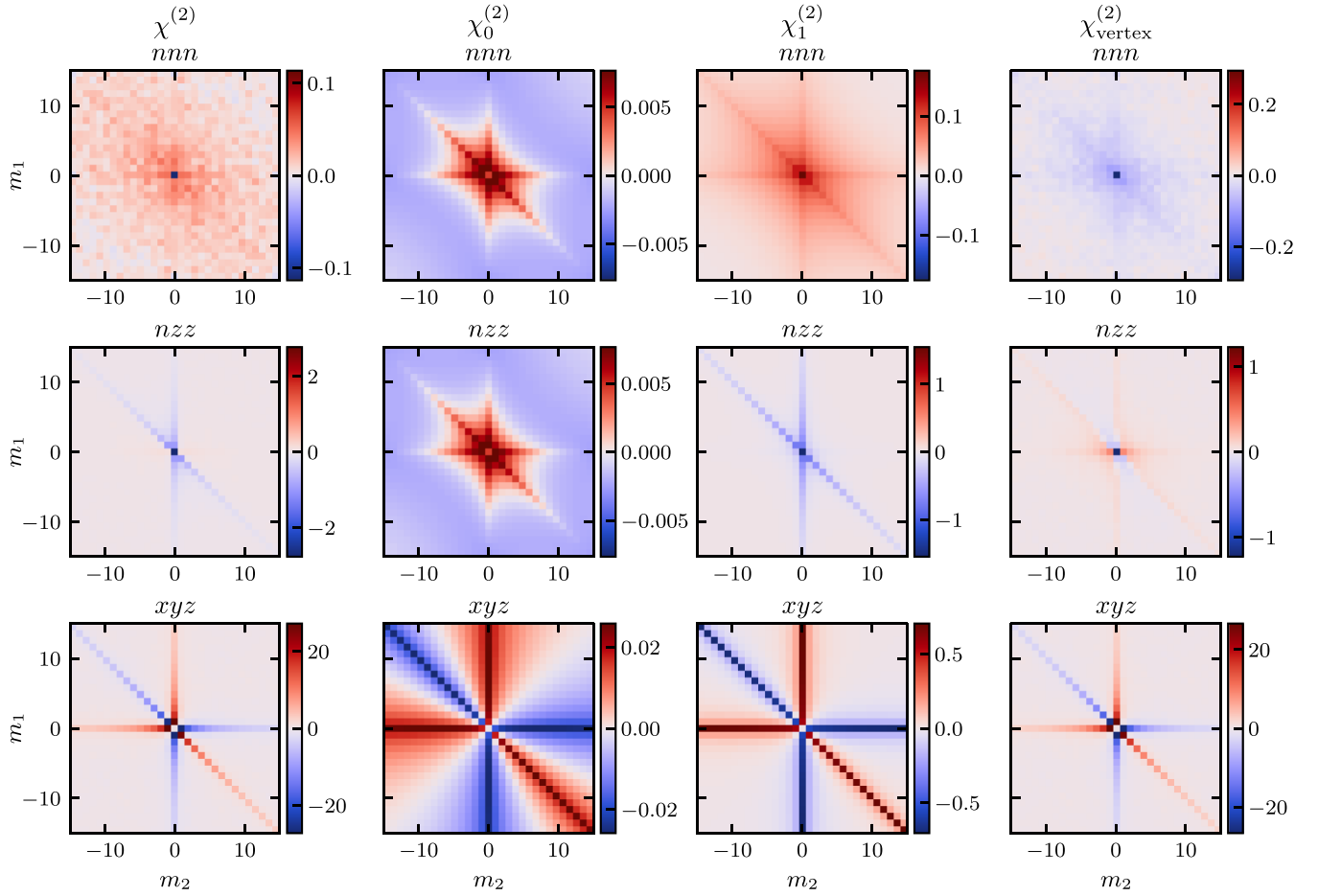
FIG. 12. Second-order response functions $\chi^{(2)}$ and their decomposition into the bubble terms $\chi_0^{(2)}$, first-order terms $\chi_1^{(2)}$, and vertex terms $\chi_{\mathrm{vertex}}^{(2)}$ in the density (nnn), density-magnetic (nzz), and chiral (xyz) channel for a single-band, square-lattice Hubbard model at $n = 1.1$, $U = 12$, and $\beta = 20$.

APPENDIX A: NONLINEAR RESPONSE THEORY

1. Nonlinear response theory in real time and frequency

We assume that the system is coupled to external classical fields $F_j(t) \in \mathbb{R}$ and $\hat{A}_j^\dagger = \hat{A}_j$ as

$$\hat{\mathcal{H}}(t) = \hat{H} - \sum_j \hat{A}_j F_j(t). \qquad (A1)$$

One example discussed in the main text is a spin $\hat{A}_j = \hat{S}_j$ coupled to a magnetic field $F_j = B_j$, where $j = x, y, z$. We furthermore assume that the dynamics of the density matrix $\hat{\rho}$ are governed by the von Neumann equation:

$$\frac{d}{dt}\hat{\rho}(t) = -i[\hat{\mathcal{H}}(t), \hat{\rho}(t)], \qquad (A2)$$

with $\hat{\rho}(t_0) = \frac{1}{Z}e^{-\beta\hat{H}} =: \hat{\rho}_0$. In the interaction picture (with respect to $\hat{H}$) the solution to the von Neumann equation can be written as an infinite series of the following form:

$$\hat{\rho}(t) = \hat{\rho}_0 + i \sum_j \int_{t_0}^t dt'\, [\hat{A}_j(t'), \hat{\rho}(t')] F_j(t')$$

$$= \hat{\rho}_0 + \sum_{\ell=1}^\infty \sum_{j_1, j_2, \ldots, j_\ell} \int_{t_0}^t dt_1 \int_{t_0}^{t_1} dt_2 \cdots \int_{t_0}^{t_{\ell-1}} dt_\ell$$

$$\times [\hat{A}_{j_1}(t_1), [\hat{A}_{j_2}(t_2), \ldots, [\hat{A}_{j_\ell}(t_\ell), \hat{\rho}_0]] \cdots]$$

$$\times F_{j_1}(t_1) F_{j_2}(t_2) \cdots F_{j_\ell}(t_\ell). \qquad (A3)$$

The expectation value of a generic operator $\langle \hat{A}_i(t) \rangle_{\mathbf{F}} = \mathrm{Tr}[\hat{\rho}(t)\hat{A}_i(t)]$ can now be evaluated in a straightforward way. It is convenient to use a matrix identity:

$$\mathrm{Tr}([\hat{A}_1, [\hat{A}_2, \ldots, [\hat{A}_\ell, \hat{\rho}_0] \cdots]]\hat{A}_i)$$

$$= \mathrm{Tr}([[\cdots [\hat{A}_i, \hat{A}_1], \hat{A}_2], \ldots, \hat{A}_\ell] \hat{\rho}_0). \qquad (A4)$$

This allows us to express the expectation value $\langle \hat{A}_i(t) \rangle$ as

$$
\langle \hat{A}_i(t) \rangle_{\mathbf{F}} = \langle \hat{A} \rangle_{\mathbf{F}=0} + \sum_{\ell=1}^{\infty} \langle \Delta \hat{A}_i(t) \rangle^{(\ell)}
$$

$$
:= \langle \hat{A} \rangle_{\mathbf{F}=0} + \sum_{\ell=1}^{\infty} \sum_{j_1 j_2,\ldots,j_\ell} \int_{-\infty}^{\infty} dt_1 \int_{-\infty}^{\infty} dt_2 \cdots \int_{-\infty}^{\infty} dt_\ell
$$

$$
\times F_{j_1}(t_1) F_{j_2}(t_2) \cdots F_{j_\ell}(t_\ell) \chi_{j_1 j_2,\ldots,j_\ell i}^{R}(t_1, t_2, \ldots, t_\ell, t),
$$
(A5)

where the (generalized) Kubo susceptibility is

$$
\chi_{j_1 j_2,\ldots,j_\ell i}^{R}(t_1, t_2, \ldots, t_\ell, t)
$$
$$
= i^{\ell} \, \theta_{t > t_1 > t_2 > \ldots > t_\ell > t_0}
$$
$$
\times \langle [[\cdots [\hat{A}_i(t), \hat{A}_{j_1}(t_1)], \hat{A}_{j_2}(t_2)], \ldots, \hat{A}_{j_\ell}(t_\ell)] \rangle. \quad \text{(A6)}
$$

Kubo already remarked in [24] [Eqs. (2.28) and (2.29)] that his formalism is not limited to linear response theory. Nonetheless, we call the quantity in Eq. (A6) generalized Kubo susceptibility (although the generalization was done already by Kubo himself in the original work).

For the Fourier transform, it is convenient to assume $F_i(t < t_0) = 0$, i.e., that the field is only switched on for positive times. The Fourier transform of a contribution of order ℓ in the external field F enjoys the representation given in Eq. (A7),

$$
\langle \Delta \hat{A}_i(\omega) \rangle^{(\ell)} = \frac{1}{(2\pi)^{\ell-1}} \int_{-\infty}^{\infty} d\omega_1 \int_{-\infty}^{\infty} d\omega_2 \cdots \int_{-\infty}^{\infty} d\omega_\ell
$$

$$
\times \delta\left(\omega - \sum_{i=1}^{\ell} \omega_i \right) F_{j_1}(\omega_1) F_{j_2}(\omega_2) \cdots F_{j_\ell}(\omega_\ell)
$$

$$
\times \chi_{j_1 j_2,\ldots,j_\ell i}^{R}(-\omega_1, -\omega_2, \ldots, -\omega_\ell, t = 0),
$$
(A7)

which predicts higher-order harmonics generation for $\ell > 1$.

In the following, we give the equivalent expressions of Eqs. (A1)–(A6) in imaginary times and frequencies.

2. Nonlinear response theory in imaginary time and frequency

Similar derivations are found in standard textbooks such as Ref. [46] (Chap. 7.2). In fact, we follow [46] for the most part, but keep the terms of higher order.

In imaginary time, the Hamiltonian is given as

$$
\hat{\mathcal{H}}(\tau) = \hat{H} - \sum_j \hat{A}_j F_j(\tau).
$$
(A8)

The analogous action is

$$
\mathcal{S}[c^+, c, \mathbf{F}] = S[c^+, c] - \sum_{jaa'} \int_0^{\beta} d\tau \, F_j(\tau) c_a^+(\tau) A_j^{aa'} c_{a'}(\tau),
$$
(A9)

where $c^+(\tau)$ and $c(\tau)$ are Grassmann-valued fields corresponding to the eigenvalues of $\hat{c}^{\dagger}(\tau)$ and $\hat{c}(\tau)$ with respect to coherent states. $A_j^{aa'}$ are matrix elements of $\hat{A}_j$: $\hat{A}_j = \sum_{aa'} \hat{c}_a^{\dagger} A_j^{aa'} \hat{c}_{a'}$. The derivation does not hinge on $\hat{A}_j$ being a one-particle operator; one can equally well assume $\hat{A}_j$ to be an arbitrary (Hermitian) n-particle operator. The expectation value $\langle \hat{A}_i(\tau) \rangle$ is best expressed in the path-integral

formalism:

$$
\langle \cdots \rangle_{\mathbf{F}} = \mathcal{Z}^{-1} \int \mathcal{D}c^+ \mathcal{D}c \, e^{-\mathcal{S}[c^+, c, \mathbf{F}]} \cdots
$$
(A10)

$$
\mathcal{Z} = \int \mathcal{D}c^+ \mathcal{D}c \, e^{-\mathcal{S}[c^+, c, \mathbf{F}]},
$$
(A11)

$$
\langle \hat{A}_i(\tau) \rangle_{\mathbf{F}} = \frac{\delta}{\delta F_i(\tau)} \ln \mathcal{Z}.
$$
(A12)

This allows us to express $\langle \hat{A}_i(\tau) \rangle_{\mathbf{F}}$ as a functional Taylor series:

$$
\langle \hat{A}_i(\tau) \rangle_{\mathbf{F}} = \sum_{\ell=0}^{\infty} \langle \Delta \hat{A}_i(\tau) \rangle_{\mathbf{F}}^{(\ell)},
$$

$$
\langle \Delta \hat{A}_i(\tau) \rangle_{\mathbf{F}}^{(\ell)} = \frac{1}{\ell!} \int_0^{\beta} d\tau_1 \int_0^{\beta} d\tau_2 \cdots \int_0^{\beta} d\tau_\ell
$$

$$
\times \sum_{j_1, j_2,\ldots,j_\ell} F_{j_1}(\tau_1) F_{j_2}(\tau_2) \cdots F_{j_\ell}(\tau_\ell)
$$

$$
\times \chi_{j_1 j_2,\ldots,j_\ell i}(\tau_1, \tau_2, \ldots, \tau_\ell, \tau),
$$
(A13)

where the $(\ell + 1)$-point susceptibility reads

$$
\chi_{j_1 j_2,\ldots,j_\ell i}(\tau_1, \tau_2, \ldots, \tau_\ell, \tau) = \frac{\delta}{\delta F_{j_1}(\tau_1)} \frac{\delta}{\delta F_{j_2}(\tau_2)} \cdots
$$

$$
\times \frac{\delta}{\delta F_{j_\ell}(\tau_\ell)} \langle \hat{A}_i(\tau) \rangle_{\mathbf{F}} \bigg|_{\mathbf{F}=0}.
$$
(A14)

All functional derivatives can be exchanged with one another. Calculating a susceptibility of order ℓ is a simple exercise in differentiation. The first-order term is the usual linear response function,

$$
\chi_{ij}(\tau, \tau') = \frac{\delta}{\delta F_i(\tau)} \frac{\delta}{\delta F_j(\tau')} \ln \mathcal{Z} \bigg|_{\mathbf{F}=0}
$$

$$
= -\mathcal{Z}^{-2} \left[\frac{\delta}{\delta F_i(\tau)} \mathcal{Z} \right] \left[\frac{\delta}{\delta F_j(\tau')} \mathcal{Z} \right] \bigg|_{\mathbf{F}=0}
$$

$$
+ \mathcal{Z}^{-1} \left[\frac{\delta}{\delta F_i(\tau)} \frac{\delta}{\delta F_j(\tau')} \mathcal{Z} \right] \bigg|_{\mathbf{F}=0}
$$

$$
= -\langle \hat{A}_i \rangle \langle \hat{A}_j \rangle + \langle T \hat{A}_i(\tau) \hat{A}_j(\tau') \rangle.
$$
(A15)

The second-order term reads

$$
\chi_{ij_1 j_2}(\tau, \tau_1, \tau_2)
$$

$$
= \frac{\delta}{\delta F_i(\tau)} \frac{\delta}{\delta F_{j_1}(\tau_1)} \frac{\delta}{\delta F_{j_2}(\tau_2)} \ln \mathcal{Z} \bigg|_{\mathbf{F}=0}
$$

$$
= 2\mathcal{Z}^{-3} \left[\frac{\delta}{\delta F_i(\tau)} \mathcal{Z} \right] \left[\frac{\delta}{\delta F_{j_1}(\tau_1)} \mathcal{Z} \right] \left[\frac{\delta}{\delta F_{j_2}(\tau_2)} \mathcal{Z} \right] \bigg|_{\mathbf{F}=0}
$$

$$
- \mathcal{Z}^{-2} \left[\frac{\delta}{\delta F_i(\tau)} \mathcal{Z} \right] \left[\frac{\delta}{\delta F_{j_1}(\tau_1)} \frac{\delta}{\delta F_{j_2}(\tau_2)} \mathcal{Z} \right] \bigg|_{\mathbf{F}=0}
$$

$$
- \mathcal{Z}^{-2} \left[\frac{\delta}{\delta F_{j_1}(\tau_1)} \mathcal{Z} \right] \left[\frac{\delta}{\delta F_i(\tau)} \frac{\delta}{\delta F_{j_2}(\tau_2)} \mathcal{Z} \right] \bigg|_{\mathbf{F}=0}
$$

$$
- \mathcal{Z}^{-2} \left[\frac{\delta}{\delta F_{j_2}(\tau_2)} \mathcal{Z} \right] \left[\frac{\delta}{\delta F_i(\tau)} \frac{\delta}{\delta F_{j_1}(\tau_1)} \mathcal{Z} \right] \bigg|_{\mathbf{F}=0}
$$

$$
+ \mathcal{Z}^{-1} \left[\frac{\delta}{\delta F_i(\tau)} \frac{\delta}{\delta F_{j_1}(\tau_1)} \frac{\delta}{\delta F_{j_2}(\tau_2)} \mathcal{Z} \right] \bigg|_{\mathbf{F}=0}
$$

$$= +2\langle \hat{A}_i\rangle\langle \hat{A}_{j_1}\rangle\langle \hat{A}_{j_2}\rangle$$
$$- \langle \hat{A}_i\rangle\langle T\hat{A}_{j_1}(\tau_1)\hat{A}_{j_2}(\tau_2)\rangle$$
$$- \langle \hat{A}_{j_1}\rangle\langle T\hat{A}_i(\tau)\hat{A}_{j_2}(\tau_2)\rangle$$
$$- \langle \hat{A}_{j_2}\rangle\langle T\hat{A}_i(\tau)\hat{A}_{j_1}(\tau_1)\rangle$$
$$+ \langle T\hat{A}_i(\tau)\hat{A}_{j_1}(\tau_1)\hat{A}_{j_2}(\tau_2)\rangle, \tag{A16}$$

which after some reordering and plugging into Eq. (A15) can be written as

$$\chi_{ij_1j_2}(\tau, \tau_1, \tau_2) = \langle T\hat{A}_i(\tau)\hat{A}_{j_1}(\tau_1)\hat{A}_{j_2}(\tau_2)\rangle$$
$$- \langle \hat{A}_i\rangle\chi_{j_1j_2}(\tau_1, \tau_2) - \langle \hat{A}_{j_1}\rangle\chi_{ij_2}(\tau, \tau_2)$$
$$- \langle \hat{A}_{j_2}\rangle\chi_{ij_1}(\tau, \tau_1) - \langle \hat{A}_i\rangle\langle \hat{A}_{j_1}\rangle\langle \hat{A}_{j_2}\rangle. \tag{A17}$$

Equations (A15)–(A17) conclude the derivation of Eqs. (2) and (3) in the main text.

APPENDIX B: IMPLEMENTATION DETAILS FOR THREE-PARTICLE CORRELATORS AND SECOND-ORDER RESPONSE FUNCTIONS

In this Appendix, we present all the details and explicit equations, purposefully omitted for brevity in Sec. II, to get from two- and three-particle correlators to the second-order density, density-magnetic, and chiral response functions. This is interesting if one actually wants to implement the computations since, in our case, w2dynamics can only directly measure the spin correlators.

We start by giving explicit formulas for Eq. (12),

$$\chi_{nnn} = 2(\chi_{\uparrow\uparrow\uparrow} + \chi_{\uparrow\uparrow\downarrow} + \chi_{\uparrow\downarrow\uparrow} + \chi_{\downarrow\uparrow\uparrow}), \tag{B1}$$

$$\chi_{nzz} = 2(\chi_{\uparrow\uparrow\uparrow} - \chi_{\uparrow\uparrow\downarrow} - \chi_{\uparrow\downarrow\uparrow} + \chi_{\downarrow\uparrow\uparrow})$$
$$= 2(\chi_{\uparrow\overline{\uparrow\downarrow}} + \chi_{\downarrow\overline{\uparrow\downarrow}}), \tag{B2}$$

$$\chi_{xyz} = 2i(\chi_{\overline{\uparrow\downarrow}\uparrow} - \chi_{\overline{\uparrow\downarrow}\downarrow}), \tag{B3}$$

where we use SU(2) symmetry, introduce the second-order spin susceptibilities

$$\chi_{\sigma_1,...,\sigma_6} = \text{conn}\, X_{\sigma_1,...,\sigma_6}, \tag{B4}$$

and generalize the compact spin notation from the two- to the three-particle level:

$$\sigma_1\sigma_2\sigma_3 = \sigma_1\sigma_1\sigma_2\sigma_2\sigma_3\sigma_3, \tag{B5}$$

$$\sigma_1\overline{\sigma_2\sigma_3} = \sigma_1\sigma_1\sigma_2\sigma_3\sigma_3\sigma_2, \tag{B6}$$

$$\overline{\sigma_1}\sigma_2\overline{\sigma_3} = \sigma_1\sigma_3\sigma_2\sigma_2\sigma_3\sigma_1, \tag{B7}$$

$$\overline{\sigma_1\sigma_2}\sigma_3 = \sigma_1\sigma_2\sigma_2\sigma_1\sigma_3\sigma_3. \tag{B8}$$

Since subtracting the disconnected parts of the full correlators is a linear operation, Eqs. (B1)–(B3) also hold when replacing χ with X.

Appendix G shows that the 20 nonvanishing spin components of the three-particle quantities can be reduced to just three independent ones, namely $\uparrow\uparrow\uparrow$, $\uparrow\uparrow\downarrow$, and $\uparrow\overline{\uparrow\downarrow}$. All

other components can be calculated from these by applying SU(2), swapping, or time-reversal symmetry. This makes numerical computations much cheaper. Exploiting this, we rewrite Eqs. (B1)–(B3) in Matsubara space as

$$\chi_{nnn}^{\omega_1\omega_2} = 2\big(\chi_{\uparrow\uparrow\uparrow}^{\omega_1\omega_2} + \chi_{\uparrow\uparrow\downarrow}^{\omega_1\omega_2} + \chi_{\uparrow\uparrow\downarrow}^{\omega_1\omega_3} + \chi_{\uparrow\uparrow\downarrow}^{\omega_3\omega_2}\big), \tag{B9}$$

$$\chi_{nzz}^{\omega_1\omega_2} = 2\big(\chi_{\uparrow\uparrow\uparrow}^{\omega_1\omega_2} - \chi_{\uparrow\uparrow\downarrow}^{\omega_1\omega_2} - \chi_{\uparrow\uparrow\downarrow}^{\omega_1\omega_3} + \chi_{\uparrow\uparrow\downarrow}^{\omega_3\omega_2}\big)$$
$$= 2\big(\chi_{\uparrow\uparrow\downarrow}^{\omega_1\omega_2} + \chi_{\uparrow\uparrow\downarrow}^{\omega_1\omega_3}\big), \tag{B10}$$

$$\chi_{xyz}^{\omega_1\omega_2} = 2i\big(\chi_{\uparrow\uparrow\downarrow}^{\omega_3\omega_1} - \chi_{\uparrow\uparrow\downarrow}^{\omega_3\omega_2}\big), \tag{B11}$$

where $\omega_3 = -\omega_1 - \omega_2$.

For the second-order spin susceptibilities, the explicit form of Eq. (5) reads

$$\chi_{\sigma_1\sigma_2\sigma_3}^{\omega_1\omega_2} = X_{\sigma_1\sigma_2\sigma_3}^{\omega_1\omega_2} - \delta_{\omega_1 0}\delta_{\omega_2 0}\beta^2\langle\hat{n}_{\sigma_1}\rangle\langle\hat{n}_{\sigma_2}\rangle\langle\hat{n}_{\sigma_3}\rangle$$
$$- \delta_{\omega_2 0}\beta\langle\hat{n}_{\sigma_2}\rangle\chi_{\sigma_3\sigma_1}^{\omega_3} - \delta_{\omega_3 0}\beta\langle\hat{n}_{\sigma_3}\rangle\chi_{\sigma_1\sigma_2}^{\omega_1}$$
$$- \delta_{\omega_1 0}\beta\langle\hat{n}_{\sigma_1}\rangle\chi_{\sigma_2\sigma_3}^{\omega_2}, \tag{B12}$$

$$\chi_{\sigma_1\overline{\sigma_2\sigma_3}}^{\omega_1\omega_2} = X_{\sigma_1\overline{\sigma_2\sigma_3}}^{\omega_1\omega_2} - \delta_{\omega_1 0}\beta\langle\hat{n}_{\sigma_1}\rangle\chi_{\overline{\sigma_3\sigma_2}}^{\omega_2}, \tag{B13}$$

$$\chi_{\overline{\sigma_1}\sigma_2\overline{\sigma_3}}^{\omega_1\omega_2} = X_{\overline{\sigma_1}\sigma_2\overline{\sigma_3}}^{\omega_1\omega_2} - \delta_{\omega_2 0}\beta\langle\hat{n}_{\sigma_2}\rangle\chi_{\overline{\sigma_1\sigma_3}}^{\omega_3}, \tag{B14}$$

$$\chi_{\overline{\sigma_1\sigma_2}\sigma_3}^{\omega_1\omega_2} = X_{\overline{\sigma_1\sigma_2}\sigma_3}^{\omega_1\omega_2} - \delta_{\omega_3 0}\beta\langle\hat{n}_{\sigma_3}\rangle\chi_{\overline{\sigma_2\sigma_1}}^{\omega_1}. \tag{B15}$$

Similarly, using Eq. (4) yields

$$\chi_{\sigma_1\sigma_2}^{\omega} = \langle T\hat{n}_{\sigma_1}\hat{n}_{\sigma_2}\rangle^{\omega} - \delta_{\omega 0}\beta\langle\hat{n}_{\sigma_1}\rangle\langle\hat{n}_{\sigma_2}\rangle, \tag{B16}$$

$$\chi_{\overline{\sigma_1\sigma_2}}^{\omega} = \langle T\hat{c}_{\sigma_1}^\dagger\hat{c}_{\sigma_2}\hat{c}_{\sigma_2}^\dagger\hat{c}_{\sigma_1}\rangle^{\omega} \tag{B17}$$

for the linear spin susceptibilities. Together these equations complete the set of explicit formulas necessary to compute the second-order density, density-magnetic, and chiral response functions from two- and three-particle spin correlators.

Combining Eqs. (B3) and (B15) shows that the disconnected terms for χ_{xyz} cancel, which means that it is directly given by X_{xyz}. This is similar to the two-particle case in which the magnetic response function χ_{zz} equals the full correlator $X_{zz} = \langle T\hat{\sigma}_z\hat{\sigma}_z\rangle$ [see Eq. (17)] because there are no disconnected terms either.
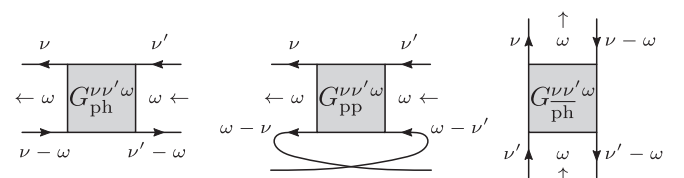

FIG. 13. Frequency notations for the two-particle Green's function.

TABLE I. The 15 different frequency notations of three-particle diagrams.

Channel	ν_1	ν_2	ν_3	ν_4	ν_5	ν_6
ph	$\nu_a - \omega_a$	ν_a	$\nu_b - \omega_b$	ν_b	$\nu_c - \omega_c$	ν_c
ph$'$	$\nu_c - \omega_c'$	ν_a	$\nu_a - \omega_a'$	ν_b	$\nu_b - \omega_b'$	ν_c
$\overline{ph}$	$\nu_b - \overline{\omega}_b$	ν_a	$\nu_c - \overline{\omega}_c$	ν_b	$\nu_a - \overline{\omega}_a$	ν_c
ph$_{\overline{a}}$	$\nu_c - \omega_c'$	ν_a	$\nu_b - \omega_b$	ν_b	$\nu_a - \overline{\omega}_a$	ν_c
ph$_{\overline{b}}$	$\nu_b - \overline{\omega}_b$	ν_a	$\nu_a - \omega_a'$	ν_b	$\nu_c - \omega_c$	ν_c
ph$_{\overline{c}}$	$\nu_a - \omega_a$	ν_a	$\nu_c - \overline{\omega}_c$	ν_b	$\nu_b - \omega_b'$	ν_c
pp$_{24-13}$	ν_c	ν_a	$\nu_b - \omega_b$	ν_b	$\omega_c - \nu_c$	$\omega_a - \nu_a$
pp$_{26-13}$	ν_a	$\omega_c - \nu_c$	$\omega_a - \nu_a$	ν_b	$\nu_b - \omega_b'$	ν_c
pp$_{26-15}$	$\omega_a - \nu_a$	$\omega_b - \nu_b$	ν_a	ν_b	$\nu_c - \omega_c$	ν_c
pp$_{46-15}$	$\nu_c - \omega_c'$	ν_a	ν_b	$\omega_a - \nu_a$	$\omega_b - \nu_b$	ν_c
pp$_{46-35}$	$\nu_a - \omega_a$	ν_a	$\omega_b - \nu_b$	$\omega_c - \nu_c$	ν_b	ν_c
pp$_{24-35}$	$\omega_c - \nu_c$	ν_a	$\nu_a - \omega_a'$	ν_b	ν_c	$\omega_b - \nu_b$
pp$_{26-35}$	ν_c	ν_a	$\omega_c - \nu_c$	ν_b	$\nu_a - \overline{\omega}_a$	$\omega_b - \nu_b$
pp$_{46-13}$	$\nu_b - \overline{\omega}_b$	$\omega_c - \nu_c$	ν_a	ν_b	$\omega_a - \nu_a$	ν_c
pp$_{24-15}$	$\omega_b - \nu_b$	ν_a	$\nu_c - \overline{\omega}_c$	$\omega_a - \nu_a$	ν_b	ν_c

In the special case of half-filling, i.e., $\langle \hat{n}_\sigma \rangle = 1/2 = 1 - \langle \hat{n}_\sigma \rangle$, we can further compute

$$X_{\sigma_1 \sigma_2 \sigma_3} = \langle T(1 - \hat{n}_{\sigma_1})(1 - \hat{n}_{\sigma_2})(1 - \hat{n}_{\sigma_3}) \rangle \quad \text{(B18)}$$

$$= \langle 1 - \hat{n}_{\sigma_1} - \hat{n}_{\sigma_2} - \hat{n}_{\sigma_3} \rangle$$
$$+ \langle T(\hat{n}_{\sigma_1}\hat{n}_{\sigma_2} + \hat{n}_{\sigma_1}\hat{n}_{\sigma_3} + \hat{n}_{\sigma_2}\hat{n}_{\sigma_3}) \rangle$$
$$- \langle T\hat{n}_{\sigma_1}\hat{n}_{\sigma_2}\hat{n}_{\sigma_3} \rangle, \quad \text{(B19)}$$

$$2X_{\sigma_1 \sigma_2 \sigma_3} = \sum_{i<j} \langle T\hat{n}_{\sigma_i}\hat{n}_{\sigma_j} \rangle - \frac{1}{2}. \quad \text{(B20)}$$

This shows that the full, density-like, three-particle spin correlators only consist of disconnected terms for half-filling, or equivalently $\chi_{\sigma_1 \sigma_2 \sigma_3}$ vanishes. Looking at Eqs. (B1) and (B2), this also implies that the second-order density and density-magnetic response functions vanish at half-filling.
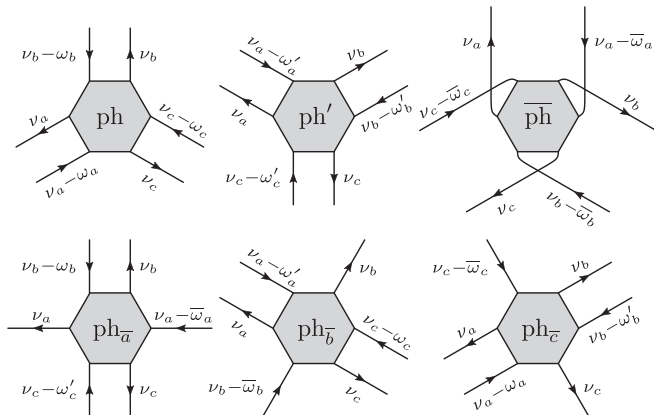
APPENDIX C: FREQUENCY NOTATIONS OF THREE-PARTICLE DIAGRAMS

In the two-particle case, there are three channels each with its own frequency notation. It is chosen such that the in- and outgoing particle-particle (pp) or particle-hole (ph) pairs have a total energy of ω. The corresponding diagrams for the two-particle Green's function are shown in Fig. 13.

Making similar pairwise connections as in Fig. 13, the number of different frequency notations for an n-particle function is equal to the number of different ways that the $2n$ points can be connected into pairs. This number of possibilities p is

FIG. 14. Diagrammatic representation of the six ph notations of three-particle diagrams.
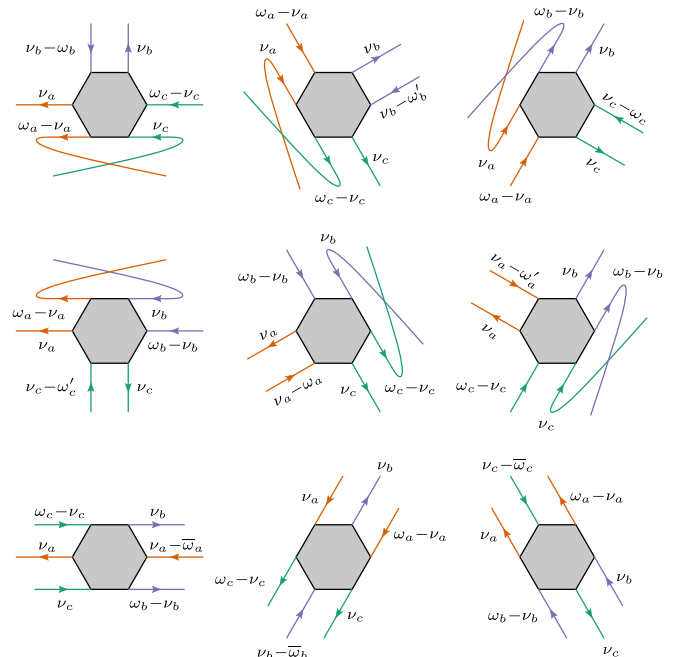

FIG. 15. Diagrammatic representation of the nine pp notations of three-particle diagrams.
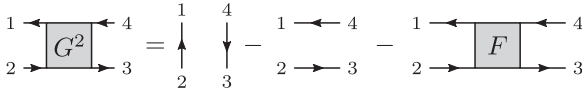
FIG. 16. Diagrammatic representation of the decomposition of the two-particle Green's function G^2, as given in Eq. (D2). The last term introduces the full two-particle vertex F.

given by the double factorial

$$p(n) = (2n - 1)!! = \prod_{k=1}^{n} (2k - 1), \qquad (C1)$$

because with $2k$ remaining points there are $2k - 1$ possibilities to connect an arbitrarily chosen point to one of the $2k - 1$ other ones. The number of pure ph channels is $n!$ since in this case each of the n creation operators must be paired with one of the n annihilation operators and there are $n!$ unique ways to do that.

For the three-particle case, this results in 15 different frequency notations, which are shown in Table I.They can be divided into six ph channels and nine pp channels. A diagrammatic representation is given in Figs. 14 and 15, depicting the ph and pp channels, respectively.

APPENDIX D: DECOMPOSITION OF THE THREE-PARTICLE GREEN'S FUNCTION

The general idea is to decompose the expectation value of an n-particle Green's function into all possible sets of connected tuples of creation and annihilation operators. If we denote the connected tuples by underlined expectation values, the one-particle case is trivially written as

$$G_{12}^1 = -\langle T \hat{c}_1 \hat{c}_2^\dagger \rangle = -\underline{\langle T \hat{c}_1 \hat{c}_2^\dagger \rangle}, \qquad (D1)$$

where we condensed all arguments and indices of each operator into a single numeric index. On the two-particle level, we get

$$G_{1234}^2 = \langle T \hat{c}_1 \hat{c}_2^\dagger \hat{c}_3 \hat{c}_4^\dagger \rangle$$
$$= \underline{\langle T \hat{c}_1 \hat{c}_2^\dagger \hat{c}_3 \hat{c}_4^\dagger \rangle} + \underline{\langle T \hat{c}_1 \hat{c}_2^\dagger \rangle}\underline{\langle T \hat{c}_3 \hat{c}_4^\dagger \rangle} - \underline{\langle T \hat{c}_1 \hat{c}_4^\dagger \rangle}\underline{\langle T \hat{c}_3 \hat{c}_2^\dagger \rangle}, \qquad (D2)$$

where the first term on the right-hand side contains the full two-particle vertex F. The diagrammatic representation of this equation is given in Fig. 16, which also shows that we choose the following convention for the sign of F:

$$\langle T \hat{c} \hat{c}^\dagger \hat{c} \hat{c}^\dagger \rangle = -GGFGG. \qquad (D3)$$

So far this is nothing new for people who are well-versed in diagrammatics. The decomposition of the three-particle Green's function, however, is less well known and simple, which is why we explicitly present it in this Appendix. Applying the same method as before, we get

$$-\langle T \hat{c}_1 \hat{c}_2^\dagger \hat{c}_3 \hat{c}_4^\dagger \hat{c}_5 \hat{c}_6^\dagger \rangle = -\underline{\langle T \hat{c}_1 \hat{c}_2^\dagger \rangle}\underline{\langle T \hat{c}_3 \hat{c}_4^\dagger \rangle}\underline{\langle T \hat{c}_5 \hat{c}_6^\dagger \rangle} - \underline{\langle T \hat{c}_1 \hat{c}_6^\dagger \rangle}\underline{\langle T \hat{c}_3 \hat{c}_2^\dagger \rangle}\underline{\langle T \hat{c}_5 \hat{c}_4^\dagger \rangle} - \underline{\langle T \hat{c}_1 \hat{c}_4^\dagger \rangle}\underline{\langle T \hat{c}_3 \hat{c}_6^\dagger \rangle}\underline{\langle T \hat{c}_5 \hat{c}_2^\dagger \rangle}$$
$$+ \underline{\langle T \hat{c}_1 \hat{c}_2^\dagger \rangle}\underline{\langle T \hat{c}_3 \hat{c}_6^\dagger \rangle}\underline{\langle T \hat{c}_5 \hat{c}_4^\dagger \rangle} + \underline{\langle T \hat{c}_1 \hat{c}_6^\dagger \rangle}\underline{\langle T \hat{c}_3 \hat{c}_4^\dagger \rangle}\underline{\langle T \hat{c}_5 \hat{c}_2^\dagger \rangle} + \underline{\langle T \hat{c}_1 \hat{c}_4^\dagger \rangle}\underline{\langle T \hat{c}_3 \hat{c}_2^\dagger \rangle}\underline{\langle T \hat{c}_5 \hat{c}_6^\dagger \rangle}$$
$$- \underline{\langle T \hat{c}_1 \hat{c}_2^\dagger \rangle}\underline{\langle T \hat{c}_3 \hat{c}_4^\dagger \hat{c}_5 \hat{c}_6^\dagger \rangle} - \underline{\langle T \hat{c}_3 \hat{c}_4^\dagger \rangle}\underline{\langle T \hat{c}_5 \hat{c}_6^\dagger \hat{c}_1 \hat{c}_2^\dagger \rangle} - \underline{\langle T \hat{c}_5 \hat{c}_6^\dagger \rangle}\underline{\langle T \hat{c}_1 \hat{c}_2^\dagger \hat{c}_3 \hat{c}_4^\dagger \rangle}$$
$$+ \underline{\langle T \hat{c}_1 \hat{c}_4^\dagger \rangle}\underline{\langle T \hat{c}_3 \hat{c}_2^\dagger \hat{c}_5 \hat{c}_6^\dagger \rangle} + \underline{\langle T \hat{c}_3 \hat{c}_6^\dagger \rangle}\underline{\langle T \hat{c}_5 \hat{c}_4^\dagger \hat{c}_1 \hat{c}_2^\dagger \rangle} + \underline{\langle T \hat{c}_5 \hat{c}_2^\dagger \rangle}\underline{\langle T \hat{c}_1 \hat{c}_6^\dagger \hat{c}_3 \hat{c}_4^\dagger \rangle}$$
$$+ \underline{\langle T \hat{c}_1 \hat{c}_6^\dagger \rangle}\underline{\langle T \hat{c}_3 \hat{c}_4^\dagger \hat{c}_5 \hat{c}_2^\dagger \rangle} + \underline{\langle T \hat{c}_3 \hat{c}_2^\dagger \rangle}\underline{\langle T \hat{c}_5 \hat{c}_6^\dagger \hat{c}_1 \hat{c}_4^\dagger \rangle} + \underline{\langle T \hat{c}_5 \hat{c}_4^\dagger \rangle}\underline{\langle T \hat{c}_1 \hat{c}_2^\dagger \hat{c}_3 \hat{c}_6^\dagger \rangle}$$
$$- \underline{\langle T \hat{c}_1 \hat{c}_2^\dagger \hat{c}_3 \hat{c}_4^\dagger \hat{c}_5 \hat{c}_6^\dagger \rangle}. \qquad (D4)$$

The corresponding diagrams are depicted in Fig. 17, where we introduce the full three-particle vertex F^3. Its sign is chosen as

$$-\langle T \hat{c}_1 \hat{c}_2^\dagger \hat{c}_3 \hat{c}_4^\dagger \hat{c}_5 \hat{c}_6^\dagger \rangle = GGGF^3GGG. \qquad (D5)$$

Looking at Fig. 17, it might seem that some diagrams are "obviously" missing, but they are in fact just topologically equivalent to some of the already present ones. Examples for this are shown in Fig. 18.

APPENDIX E: ASYMPTOTIC BEHAVIOR OF $\chi^{(2)}$

Using the Lehmann representation, one can show that bosonic, two-particle correlation functions can be expanded in the following series:

$$\langle \hat{A}_i \hat{A}_j \rangle^z = -\frac{1}{z} \langle [\hat{A}_i, \hat{A}_j] \rangle + \frac{1}{z^2} \langle [[\hat{A}_i, \hat{H}], \hat{A}_j] \rangle + \cdots, \qquad (E1)$$

where z is a complex frequency, $\hat{H}$ is the Hamiltonian, and $[\cdot, \cdot]$ denotes the commutator (see also Ref. [37], Appendix C). Since

$$\chi_{nnn}^{0\omega} = -\frac{\partial}{\partial \epsilon} \chi_{nn}^\omega = \frac{\partial}{\partial \epsilon} \left(X_{nn}^\omega - \delta_{\omega 0} \beta \langle \hat{n} \rangle^2 \right) \qquad (E2)$$

$$= \frac{\partial}{\partial \epsilon} X_{nn}^\omega, \qquad (E3)$$

$$\chi_{nzz}^{0\omega} = \frac{\partial}{\partial \epsilon} \chi_{zz}^\omega = \frac{\partial}{\partial \epsilon} X_{zz}^\omega, \qquad (E4)$$

$$\chi_{xyz}^{0\omega} = \frac{\partial}{\partial h_x} \chi_{yz}^\omega = \frac{\partial}{\partial h_x} X_{yz}^\omega, \qquad (E5)$$

with Matsubara frequencies ω, evaluating the expansion at $z = i\omega$ can be used to obtain the asymptotic behavior of slices
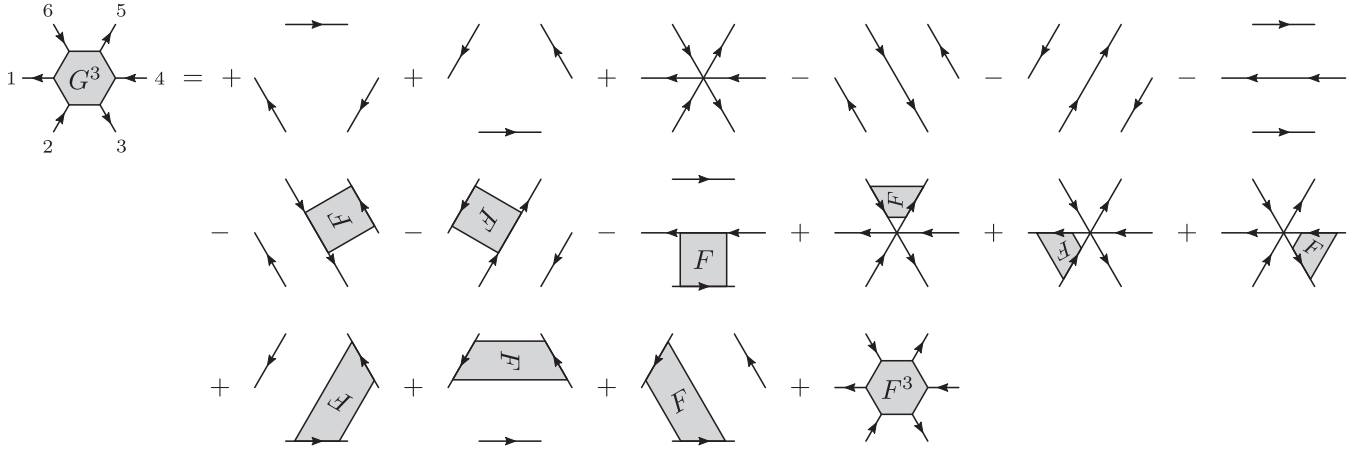
FIG. 17. Diagrammatic representation of the decomposition of the three-particle Green's function as given in Eq. (D4). The last term introduces the full three-particle vertex F^3.

of the second-order response functions:

$$\chi_{nnn}^{0\omega} \approx -\frac{1}{(i\omega)^2}\frac{\partial}{\partial \epsilon}\langle[[\hat{n},\hat{H}],\hat{n}]\rangle, \tag{E6}$$

$$\chi_{nzz}^{0\omega} \approx -\frac{1}{(i\omega)^2}\frac{\partial}{\partial \epsilon}\langle[[\hat{\sigma}_z,\hat{H}],\hat{\sigma}_z]\rangle, \tag{E7}$$

$$\chi_{xyz}^{0\omega} \approx -\frac{1}{i\omega}\frac{\partial}{\partial h_x}\langle[\hat{\sigma}_y,\hat{\sigma}_z]\rangle. \tag{E8}$$

The density and density-magnetic channels do not have a $1/(i\omega)$ term since $[\hat{n},\hat{n}]$ and $[\hat{\sigma}_z,\hat{\sigma}_z]$ vanish. According to [37], for an AIM the commutators in Eqs. (E6) and (E7) are given by

$$\langle[[\hat{n},\hat{H}_{\text{AIM}}],\hat{n}]\rangle = \langle[[\hat{\sigma}_z,\hat{H}_{\text{AIM}}],\hat{\sigma}_z]\rangle$$
$$= -\langle\hat{H}_V\rangle = -\frac{2}{\beta}\sum_{\sigma\nu}\Delta_\sigma^\nu G_\sigma^\nu, \tag{E9}$$

where $\hat{H}_V$ is the hybridization term in the Hamiltonian of the AIM [last term in Eq. (25)], Δ_σ^ν is the hybridization function, and G_σ^ν is the one-particle Green's function of the impurity.
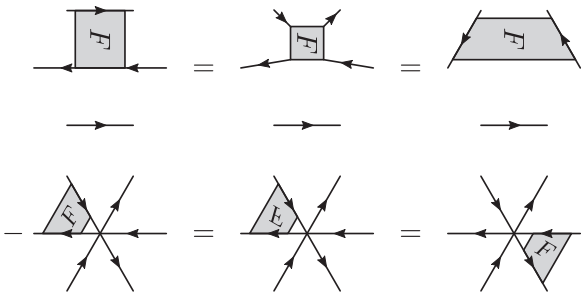

FIG. 18. Some topologically equivalent diagrams that appear in the decomposition of the three-particle Green's function shown in Fig. 17. In the second line, we use the crossing symmetry of F for the first identity.

Differentiating the latter with respect to ϵ yields

$$\frac{\partial}{\partial \epsilon}G_\sigma^\nu = -\frac{\partial}{\partial \epsilon}\langle T\hat{c}_\sigma(\tau)\hat{c}_\sigma^\dagger\rangle^\nu \tag{E10}$$

$$= \beta\langle\hat{n}\rangle G_\sigma^\nu \tag{E11}$$

$$+ \sum_{\sigma'}\langle T\hat{n}_{\sigma'}(\tau')\hat{c}_\sigma(\tau)\hat{c}_\sigma^\dagger\rangle^{\nu 0} \tag{E12}$$

$$= \beta\langle\hat{n}\rangle G_\sigma^\nu \tag{E13}$$

$$+ \sum_{\sigma'}\langle T[1-\hat{c}_{\sigma'}(\tau')\hat{c}_{\sigma'}^\dagger(\tau')]\hat{c}_\sigma(\tau)\hat{c}_\sigma^\dagger\rangle^{\nu 0} \tag{E14}$$

$$= \beta(\langle\hat{n}\rangle - 2)G_\sigma^\nu - \sum_{\sigma'}P_{\sigma'\sigma}^{\nu 0}, \tag{E15}$$

where P is the partially contracted two-particle Green's function

$$P^{\nu'\omega} = \int_0^\beta\int_0^\beta G(\tau,\tau,\tau')e^{i[\omega\tau+(\nu'-\omega)\tau']}d\tau d\tau'$$
$$= \frac{1}{\beta}\sum_\nu G^{\nu\nu'\omega}. \tag{E16}$$

With

$$\frac{\partial}{\partial h_x}\langle[\hat{\sigma}_y,\hat{\sigma}_z]\rangle = 2i\frac{\partial}{\partial h_x}\langle\hat{\sigma}_x\rangle = 2i\chi_m^0 \tag{E17}$$

we can finally write

$$\chi_{nnn}^{0\omega} \approx -\frac{1}{\omega^2}\frac{\partial}{\partial \epsilon}\langle H_V\rangle, \tag{E18}$$

$$\chi_{nzz}^{0\omega} \approx -\frac{1}{\omega^2}\frac{\partial}{\partial \epsilon}\langle H_V\rangle, \tag{E19}$$

$$\chi_{xyz}^{0\omega} \approx -\frac{2}{\omega}\chi_m^0, \tag{E20}$$

where

$$-\frac{\partial}{\partial \epsilon}\langle H_V\rangle = \frac{4}{\beta}\sum_\nu\Delta_\uparrow^\nu(P_{\uparrow\uparrow}^{\nu 0} + P_{\uparrow\downarrow}^{\nu 0} + \beta(2-\langle\hat{n}\rangle)G_\uparrow^\nu), \tag{E21}$$

and we use SU(2) symmetry.

APPENDIX F: LEHMANN FORMULA FOR THE THREE-PARTICLE CORRELATOR

In the atomic limit, $\hat{H}_{\mathrm{AL}} = \epsilon(\hat{n}_\uparrow + \hat{n}_\downarrow) - h(\hat{n}_\uparrow - \hat{n}_\downarrow) + U\hat{n}_\uparrow\hat{n}_\downarrow$, where $\epsilon = -U/2$, we use the following Lehmann formula for the three-particle correlation function:

$$X(\tau_1, \tau_2) = \langle T \hat{\rho}_1(\tau_1)\hat{\rho}_2(\tau_2)\hat{\rho}_3(0)\rangle = \theta(\tau_1 - \tau_2)\sum_{i,j,k} w_i e^{\tau_1 E_{ij} + \tau_2 E_{jk}} \rho_1^{ij}\rho_2^{jk}\rho_3^{ki} + \theta(\tau_2 - \tau_1)\sum_{i,j,k} w_i e^{\tau_2 E_{ij} + \tau_1 E_{jk}} \rho_2^{ij}\rho_1^{jk}\rho_3^{ki}. \quad \text{(F1)}$$

Here, $\hat{\rho}_{1,2,3}$ are bosonic operators, θ is the Heaviside step function, $E_{ij} = E_i - E_j$, $w_i = e^{-\beta E_i}/\mathcal{Z}$, $\mathcal{Z} = \sum_i e^{-\beta E_i}$, and $\rho^{ij} = \langle i|\hat{\rho}|j\rangle$. The eigenstates of $\hat{H}_{\mathrm{AL}}$ are $|0\rangle$, $|\downarrow\rangle$, $|\uparrow\rangle$, and $|\updownarrow\rangle$ with eigenenergies $E_0 = 0$, $E_\downarrow = \epsilon + h$, $E_\uparrow = \epsilon - h$, and $E_\updownarrow = U + 2\epsilon$.

We transform $X(\tau_1, \tau_2)$ via Eq. (24) to frequencies, taking care of degeneracies:

$$X^{\omega_1\omega_2} = \mathcal{X}(\omega_1, \omega_2, \hat{\rho}_1, \hat{\rho}_2) + \mathcal{X}(\omega_2, \omega_1, \hat{\rho}_2, \hat{\rho}_1), \quad \text{(F2)}$$

$$\begin{aligned}
\mathcal{X}(\omega_x, \omega_y, \hat{\rho}_x, \hat{\rho}_y) = \sum_{i,j,k} w_i \rho_x^{ij}\rho_y^{jk}\rho_3^{ki} \Bigg\{ & \frac{1 - \delta(i\omega_y + E_{jk})}{i\omega_y + E_{jk}} \Bigg[-\frac{e^{\beta E_{ij}} - 1}{i\omega_x + E_{ij}}[1 - \delta(i\omega_x + E_{ij})] - \beta\delta(i\omega_x + E_{ij}) \\
& + \frac{e^{\beta E_{ik}} - 1}{i\omega_x + i\omega_y + E_{ik}}[1 - \delta(i\omega_x + i\omega_y + E_{ik})] + \beta\delta(i\omega_x + i\omega_y + E_{ik}) \Bigg] \\
& + \Bigg[\frac{\beta e^{\beta E_{ij}}}{i\omega_x + E_{ij}} - \frac{e^{\beta E_{ij}} - 1}{(i\omega_x + E_{ij})^2} \Bigg]\delta(i\omega_y + E_{jk})[1 - \delta(i\omega_x + E_{ij})] + \frac{\beta^2}{2}\delta(i\omega_y + E_{jk})\delta(i\omega_x + E_{ij}) \Bigg\}. \quad \text{(F3)}
\end{aligned}$$

Note that Eqs. (F1)–(F3) are not restricted to the atomic limit.

APPENDIX G: SYMMETRIES OF THE THREE-PARTICLE SPIN CORRELATOR

There are $\binom{6}{3} = 20$ nonvanishing spin combinations for the full, three-particle correlator. With the compact spin notation introduced in Eqs. (B5)–(B8), they read

$$\begin{aligned}
& \uparrow\uparrow\uparrow, \quad \uparrow\uparrow\downarrow, \quad \uparrow\downarrow\uparrow, \quad \downarrow\uparrow\uparrow, \\
& \overline{\uparrow}\uparrow\overline{\downarrow}, \quad \uparrow\overline{\uparrow}\overline{\downarrow}, \quad \uparrow\overline{\downarrow}\overline{\uparrow}, \quad \overline{\uparrow}\overline{\downarrow}\uparrow, \quad \overline{\downarrow}\uparrow\uparrow, \quad \overline{\downarrow}\uparrow\overline{\uparrow}, \\
& \overline{\downarrow}\downarrow\overline{\uparrow}, \quad \downarrow\overline{\uparrow}\overline{\uparrow}, \quad \downarrow\overline{\uparrow}\overline{\downarrow}, \quad \overline{\downarrow}\overline{\uparrow}\downarrow, \quad \overline{\uparrow}\downarrow\downarrow, \quad \overline{\uparrow}\downarrow\overline{\downarrow}, \\
& \downarrow\downarrow\downarrow, \quad \downarrow\downarrow\uparrow, \quad \downarrow\uparrow\downarrow, \quad \uparrow\downarrow\downarrow .
\end{aligned} \quad \text{(G1)}$$

By using SU(2), swapping (SW) and time reversal (TR) symmetry,

$$X_{\sigma_1,\dots,\sigma_6}^{\omega_1\omega_2} \overset{\mathrm{SU(2)}}{=} X_{-\sigma_1,\dots,-\sigma_6}^{\omega_1\omega_2}, \quad \text{(G2)}$$

$$X_{\sigma_1,\dots,\sigma_6}^{\omega_1\omega_2} \overset{\mathrm{SW12}}{=} X_{\sigma_3\sigma_4\sigma_1\sigma_2\sigma_5\sigma_6}^{\omega_2\omega_1}, \quad \text{(G3)}$$

$$X_{\sigma_1,\dots,\sigma_6}^{\omega_1\omega_2} \overset{\mathrm{SW13}}{=} X_{\sigma_5\sigma_6\sigma_3\sigma_4\sigma_1\sigma_2}^{\omega_3\omega_1}, \quad \text{(G4)}$$

$$X_{\sigma_1,\dots,\sigma_6}^{\omega_1\omega_2} \overset{\mathrm{SW23}}{=} X_{\sigma_1\sigma_2\sigma_5\sigma_6\sigma_3\sigma_4}^{\omega_1\omega_3}, \quad \text{(G5)}$$

$$X_{\sigma_1,\dots,\sigma_6}^{\omega_1\omega_2} \overset{\mathrm{TR}}{=} X_{\sigma_6,\dots,\sigma_1}^{\omega_3\omega_2}, \quad \text{(G6)}$$

where $-\uparrow = \downarrow$, $-\downarrow = \uparrow$, and $\omega_3 = -\omega_1 - \omega_2$, they can be mapped to only three spin components, namely, $\uparrow\uparrow\uparrow$, $\uparrow\uparrow\downarrow$,

and $\uparrow\overline{\uparrow}\overline{\downarrow}$. For seven of the first ten spin components, the necessary transformations look like

$$X_{\uparrow\downarrow\uparrow}^{\omega_1\omega_2} \overset{\mathrm{SW23}}{=} X_{\uparrow\uparrow\downarrow}^{\omega_1\omega_3}, \quad \text{(G7)}$$

$$X_{\downarrow\uparrow\uparrow}^{\omega_1\omega_2} \overset{\mathrm{SW13}}{=} X_{\uparrow\uparrow\downarrow}^{\omega_3\omega_2}, \quad \text{(G8)}$$

$$X_{\overline{\uparrow}\uparrow\overline{\downarrow}}^{\omega_1\omega_2} \overset{\mathrm{SW12}}{=} X_{\uparrow\overline{\uparrow}\overline{\downarrow}}^{\omega_2\omega_1}, \quad \text{(G9)}$$

$$X_{\uparrow\overline{\downarrow}\overline{\uparrow}}^{\omega_1\omega_2} \overset{\mathrm{SW23}}{=} X_{\uparrow\overline{\uparrow}\overline{\downarrow}}^{\omega_1\omega_3}, \quad \text{(G10)}$$

$$X_{\overline{\uparrow}\overline{\downarrow}\uparrow}^{\omega_1\omega_2} \overset{\mathrm{SW23}}{=} X_{\overline{\uparrow}\uparrow\overline{\downarrow}}^{\omega_1\omega_3} \overset{\mathrm{SW12}}{=} X_{\uparrow\overline{\uparrow}\overline{\downarrow}}^{\omega_3\omega_1}, \quad \text{(G11)}$$

$$X_{\overline{\downarrow}\uparrow\uparrow}^{\omega_1\omega_2} \overset{\mathrm{SW13}}{=} X_{\uparrow\overline{\uparrow}\overline{\downarrow}}^{\omega_3\omega_2}, \quad \text{(G12)}$$

$$X_{\overline{\downarrow}\uparrow\overline{\uparrow}}^{\omega_1\omega_2} \overset{\mathrm{SW12}}{=} X_{\uparrow\overline{\downarrow}\overline{\uparrow}}^{\omega_2\omega_1} \overset{\mathrm{SW23}}{=} X_{\uparrow\overline{\uparrow}\overline{\downarrow}}^{\omega_2\omega_3}. \quad \text{(G13)}$$

Note that they are not unique. $X_{\overline{\uparrow}\downarrow\uparrow}$, e.g., can also be calculated from $X_{\uparrow\overline{\uparrow}\overline{\downarrow}}$ by applying time-reversal symmetry. These seven equations relate seven of the 20 spin components to the $\uparrow\uparrow\downarrow$ and $\uparrow\overline{\uparrow}\overline{\downarrow}$ components, and additionally we have the $\uparrow\uparrow\uparrow$ component. The second half of the 20 nonvanishing components can be mapped to the first 10 by using SU(2) symmetry.

[1] A. A. Abrikosov, L. P. Gorkov, and I. E. Dzyaloshinski, *Methods of Quantum Field Theory in Statistical Physics* (Dover, New York, 1975).

[2] W. Metzner and D. Vollhardt, Phys. Rev. Lett. **62**, 324 (1989).

[3] M. Jarrell, Phys. Rev. Lett. **69**, 168 (1992).

[4] A. Georges and G. Kotliar, Phys. Rev. B **45**, 6479 (1992).

[5] A. Georges, G. Kotliar, W. Krauth, and M. J. Rozenberg, Rev. Mod. Phys. **68**, 13 (1996).

[6] H. Kusunose, J. Phys. Soc. Jpn. **75**, 054713 (2006).

[7] A. Toschi, A. A. Katanin, and K. Held, Phys. Rev. B **75**, 045118 (2007).

[8] A. N. Rubtsov, M. I. Katsnelson, and A. I. Lichtenstein, Phys. Rev. B **77**, 033101 (2008).

[9] G. Rohringer, A. Toschi, H. Hafermann, K. Held, V. I. Anisimov, and A. A. Katanin, Phys. Rev. B **88**, 115112 (2013).

[10] C. Taranto, S. Andergassen, J. Bauer, K. Held, A. Katanin, W. Metzner, G. Rohringer, and A. Toschi, Phys. Rev. Lett. **112**, 196402 (2014).

[11] T. Ayral and O. Parcollet, Phys. Rev. B **92**, 115109 (2015).

[12] G. Li, Phys. Rev. B **91**, 165134 (2015).

[13] G. Rohringer, H. Hafermann, A. Toschi, A. A. Katanin, A. E. Antipov, M. I. Katsnelson, A. I. Lichtenstein, A. N. Rubtsov, and K. Held, Rev. Mod. Phys. **90**, 025003 (2018).

[14] G. Rohringer, A. Toschi, A. Katanin, and K. Held, Phys. Rev. Lett. **107**, 256402 (2011).

[15] A. E. Antipov, E. Gull, and S. Kirchner, Phys. Rev. Lett. **112**, 226401 (2014).

[16] D. Hirschmeier, H. Hafermann, E. Gull, A. I. Lichtenstein, and A. E. Antipov, Phys. Rev. B **92**, 144409 (2015).

[17] T. Schäfer, A. A. Katanin, K. Held, and A. Toschi, Phys. Rev. Lett. **119**, 046402 (2017).

[18] A. A. Katanin, A. Toschi, and K. Held, Phys. Rev. B **80**, 075104 (2009).

[19] T. Schäfer, F. Geles, D. Rost, G. Rohringer, E. Arrigoni, K. Held, N. Blümer, M. Aichhorn, and A. Toschi, Phys. Rev. B **91**, 125109 (2015).

[20] F. Krien, P. Worm, P. Chalupa-Gantne, A. Toschi, and K. Held, Coummun. Phys. **5**, 336 (2022).

[21] J. Otsuki, H. Hafermann, and A. I. Lichtenstein, Phys. Rev. B **90**, 235132 (2014).

[22] M. Kitatani, N. Tsuji, and H. Aoki, Phys. Rev. B **92**, 085104 (2015).

[23] T. Ribic, P. Gunacker, S. Iskakov, M. Wallerberger, G. Rohringer, A. N. Rubtsov, E. Gull, and K. Held, Phys. Rev. B **96**, 235127 (2017).

[24] R. Kubo, J. Phys. Soc. Jpn. **12**, 570 (1957).

[25] A. Jorio, R. Saito, G. Dresselhaus, and M. S. Dresselhaus, Quantum description of raman scattering, in *Raman Spectroscopy in Graphene Related Systems* (Wiley-Blackwell, Hoboken, New Jersey, 2011), Chap. 5, pp. 103–119.

[26] H. Rostami, M. I. Katsnelson, and M. Polini, Phys. Rev. B **95**, 035416 (2017).

[27] M. Vandelli, M. I. Katsnelson, and E. A. Stepanov, Phys. Rev. B **99**, 165432 (2019).

[28] H. Rostami, M. I. Katsnelson, G. Vignale, and M. Polini, Ann. Phys. **431**, 168523 (2021).

[29] Y. Michishita and R. Peters, Phys. Rev. B **103**, 195133 (2021).

[30] A. Kofuji, Y. Michishita, and R. Peters, Phys. Rev. B **104**, 085151 (2021).

[31] H. Hafermann, K. R. Patton, and P. Werner, Phys. Rev. B **85**, 205106 (2012).

[32] H. Hafermann, Phys. Rev. B **89**, 235128 (2014).

[33] P. Gunacker, M. Wallerberger, T. Ribic, A. Hausoel, G. Sangiovanni, and K. Held, Phys. Rev. B **94**, 125153 (2016).

[34] A. Moutenet, W. Wu, and M. Ferrero, Phys. Rev. B **97**, 085117 (2018).

[35] J. Kaufmann, P. Gunacker, A. Kowalski, G. Sangiovanni, and K. Held, Phys. Rev. B **100**, 075119 (2019).

[36] L. Kelvin, *Baltimore Lectures on Molecular Dynamics and the Wave Theory of Light* (C. J. Clay and Sons, London, 1904).

[37] F. Krien, E. G. C. P. van Loon, H. Hafermann, J. Otsuki, M. I. Katsnelson, and A. I. Lichtenstein, Phys. Rev. B **96**, 075155 (2017).

[38] M. Wallerberger, A. Hausoel, P. Gunacker, A. Kowalski, N. Parragh, F. Goth, K. Held, and G. Sangiovanni, Comput. Phys. Commun. **235**, 388 (2019).

[39] E. Gull, A. J. Millis, A. I. Lichtenstein, A. N. Rubtsov, M. Troyer, and P. Werner, Rev. Mod. Phys. **83**, 349 (2011).

[40] S.-S. B. Lee, F. B. Kugler, and J. von Delft, Phys. Rev. X **11**, 041007 (2021).

[41] P. Kappl, w2diag, Version 0.5.0 (2022), https://gitlab.tuwien.ac.at/e138/e138-01/software/w2dynamics-tools/w2diag.

[42] P. Kappl and F. Krien, 10.48436/s8mva-42q75 (2023).

[43] D. Medvedeva, S. Iskakov, F. Krien, V. V. Mazurenko, and A. I. Lichtenstein, Phys. Rev. B **96**, 235149 (2017).

[44] A. Hewson, *The Kondo Problem to Heavy Fermions* (Cambridge University Press, Cambridge, UK, 1993).

[45] Z. Alpicheshev (private communication).

[46] A. Altland and B. D. Simons, *Condensed Matter Field Theory*, 2nd ed. (Cambridge University Press, Cambridge, UK, 2010).

Correction: Equations (B3) and (B11) contained typographical errors and have been fixed.